SEDIMENTOLOGY the journal of the International Association of Sedimentologists

Sedimentology (2026) doi: 10.1111/sed.70134

Alluvial ridge morphology on avulsing rivers

JAMES H. GEARON*,† and DOUGLAS A. EDMONDS†
*Earth, Marine & Environmental Sciences, University of North Carolina, Chapel Hill, North Carolina, USA (E-mail: jake.gearon@gmail.com)
†Earth & Atmospheric Sciences, Indiana University, Bloomington, Indiana, USA

Associate Editor: Xin Shan

ABSTRACT

Alluvial ridges are built by preferential channel-belt deposition and control river avulsions, yet a systematic analysis of their morphology has been missing. To address this gap, we analyse a globally distributed dataset of 8970 alluvial ridge flanks on 14 different rivers. We establish that ridge height scales sub-linearly with width ($H_{AR} \propto W_{AR}^{0.75}$), indicating that ridges widen faster than they increase in height. Ridge dimensions also scale with the channel. Ridge height inversely scales with depth ($H_{AR} \propto H_M^{-0.25}$), implying that on deep channels ridges are proportionally smaller relative to channel size. Because H_{AR} decreases with increasing H_M, deeper channels are less prone to superelevation. This geometric constraint helps explain the downstream shift in avulsion potential where upstream reaches are controlled by superelevation, and downstream reaches are increasingly governed by gradient advantage. We also characterise ridge flank shapes and show that concave flanks are the most common form. However, the prevalence of convex and quasi-linear shapes demonstrates that no single idealised profile can capture the near-channel topography that guides overbank flow. These morphologic scaling laws provide a new systematic description of how alluvial ridge geometry varies across avulsing river systems and how that geometry connects to the downstream evolution of avulsion potential.

Keywords Alluvial ridges, gradient advantage, natural levees, overbank deposition, river avulsion, superelevation.

INTRODUCTION

Alluvial ridges are elevated landforms built by preferential sediment deposition within a channel belt (Fisk, 1944; Allen, 1965). The resulting topography archives the time-integrated behaviour of channel dynamics and influences river routing by initiating avulsions and guiding them across floodplains (Mohrig *et al.*, 2000; Edmonds *et al.*, 2016; Gearon *et al.*, 2024). For millennia, the well-drained soils of these ridges have also attracted human settlements, making them critical sites for archaeological inquiry (Piovan *et al.*, 2012; Kidder & Liu, 2017). Ridge cross-sectional morphology varies widely, reflecting distinct constructional processes ranging from levee-and-splay aggradation on the Río Maniqui (Lombardo, 2016) to progradational fan-delta building on the Turkwel River (Frostick & Reid, 1986).

Because ridge topography dictates river routing, it acts as a primary control on avulsion (Allen, 1965, 1978; Leeder, 1978; Bridge & Leeder, 1979; Mohrig *et al.*, 2000; Törnqvist & Bridge, 2002; Slingerland & Smith, 2004; Edmonds *et al.*, 2016; Gearon *et al.*, 2024; Gearon & Edmonds, 2025). Specifically, ridge morphology controls avulsion potential (Λ) (Gearon *et al.*, 2024), which is the product of two dimensionless ratios: superelevation (β, the ratio of ridge height H_{AR} to channel depth H_M) (Mohrig *et al.*, 2000) and gradient advantage (γ, the ratio of ridge flank slope S_{AR} to main channel slope S_M) (Slingerland & Smith, 1998). Previous global analyses established that avulsions require $\Lambda \geq 2$, with the dominant driver shifting longitudinally from β to γ downstream (Gearon *et al.*, 2024; Gearon & Edmonds, 2025). However, these studies evaluated Λ longitudinally near avulsion sites and did not examine ridge morphology and cross-sectional forms. This leaves the fundamental scaling, downstream geometric evolution and cross-sectional morphology of alluvial ridges unquantified.

To resolve this geometric gap, we quantify the morphology of 8970 individual alluvial ridge flanks extracted from a bare-earth corrected global digital elevation model (FABDEM v1.2; Hawker *et al.*, 2022). By evaluating how cross-sectional form influences avulsion potential, this analysis yields three primary findings. Firstly, at-a-station, ridges grow wider faster than they grow taller, and channel depth grows faster than ridge height. Second, channel depth and slope govern the observed downstream morphodynamic shift in avulsion potential components. Finally, ridge flank curvature spans a continuous spectrum from concave to convex, likely reflecting differences in depositional processes.

Background

Sedimentologists have used the term 'alluvial ridge' for over two centuries, but its meaning has shifted. Early 19th-century accounts used the term vaguely for any raised linear landform and often misidentified features like beach ridges as alluvial (Brown, 1817; Blowe, 1820). By the late 1800s, the term gained specificity to describe fluvially constructed topographic highs marking former river positions (Hopkins, 1884; Court, U.S.S, 1893). In the mid-20th century, Fisk's work on the Mississippi River clarified the process-based meaning of alluvial ridges (Fisk, 1944, 1952; Fisk *et al.*, 1947). He described how successive overbank floods build natural levees along a migrating river, which then coalesce into continuous topographic highs extending beyond individual meander bends (Fig. 1B). Fisk thus established natural levees as the building blocks of alluvial ridges and introduced a key temporal distinction: *levees reflect floods; ridges reflect integrated fluvial history, including migration*.

Allen later expanded this framework by linking alluvial ridge growth directly to avulsion (Allen, 1965, 1978). He argued that elevated ridges increase the likelihood of channel relocation by raising the local water level relative to the floodplain and emphasised that 'levees are largely responsible for the superelevation of alluvial ridges above the general floodplain' (Allen, 1965). Allen's linkage of ridge superelevation to avulsion led to the rule-based 'Leeder-Allen-Bridge' (LAB) models of the late 20th century. These models described how lateral channel migration, levee building and avulsion together stack channel deposits into vertically organised, mesoscale units (Allen, 1978; Leeder, 1978; Bridge & Leeder, 1979). The LAB models and their later evolutions (e.g. Mackey & Bridge, 1995; Heller & Paola, 1996; Törnqvist & Bridge, 2002; Karssenberg & Bridge, 2008; Martin & Edmonds, 2022) treated the alluvial ridge as the atomic sedimentary unit of fluvial basins, where ridge construction modulates avulsion, the primary driver of vertical stacking.

Subsequent research dissected the internal complexity of these ridges and revealed formative processes beyond simple levee aggradation, consistent with the original assertion by Fisk. Smith *et al.* (1989), for example, detailed how crevasse splays evolve through multiple stages into channel networks that construct new avulsion belts (Fig. 1C). Mohrig *et al.* (2000) later emphasised that this growth forces the channel to aggrade its bed and banks above the floodplain; the resulting elevation difference drives avulsion (Fig. 1D). Gouw (2007) formalised the cross-sectional geometry of alluvial ridges in fluvio-deltaic settings, highlighting that neither gradient advantage nor superelevation alone explains avulsion. Van Toorenenburg *et al.* (2018) highlighted the life cycle of crevasse splays as a key ridge-building mechanism, and studies of ancient successions have deciphered the genetic links among overbank deposition, ridge growth and avulsion (Hajek & Straub, 2017; Lee & Gihm, 2023) (Fig. 1E to H).

Because these depositional processes dictate the final landform, the resulting ridge geometry is deeply linked to the avulsion cycle (Smith *et al.*, 1989; Mohrig *et al.*, 2000; Törnqvist & Bridge, 2002). Empirically, the lateral extent of ridges governs avulsion pathfinding (Edmonds *et al.*, 2016), while ridge topography maintains kilometre-scale downstream correlations (Gearon & Edmonds, 2025). Complementing these field-derived metrics, numerical models constrain the underlying physical controls on ridge formation (Hajek & Wolinsky, 2012; Hajek & Straub, 2017; Nicholas *et al.*, 2018).

Despite this conceptual progress, a cohesive, quantitative understanding of alluvial ridge morphology remains elusive. For nearly a century, the knowledge was built on only a few site-

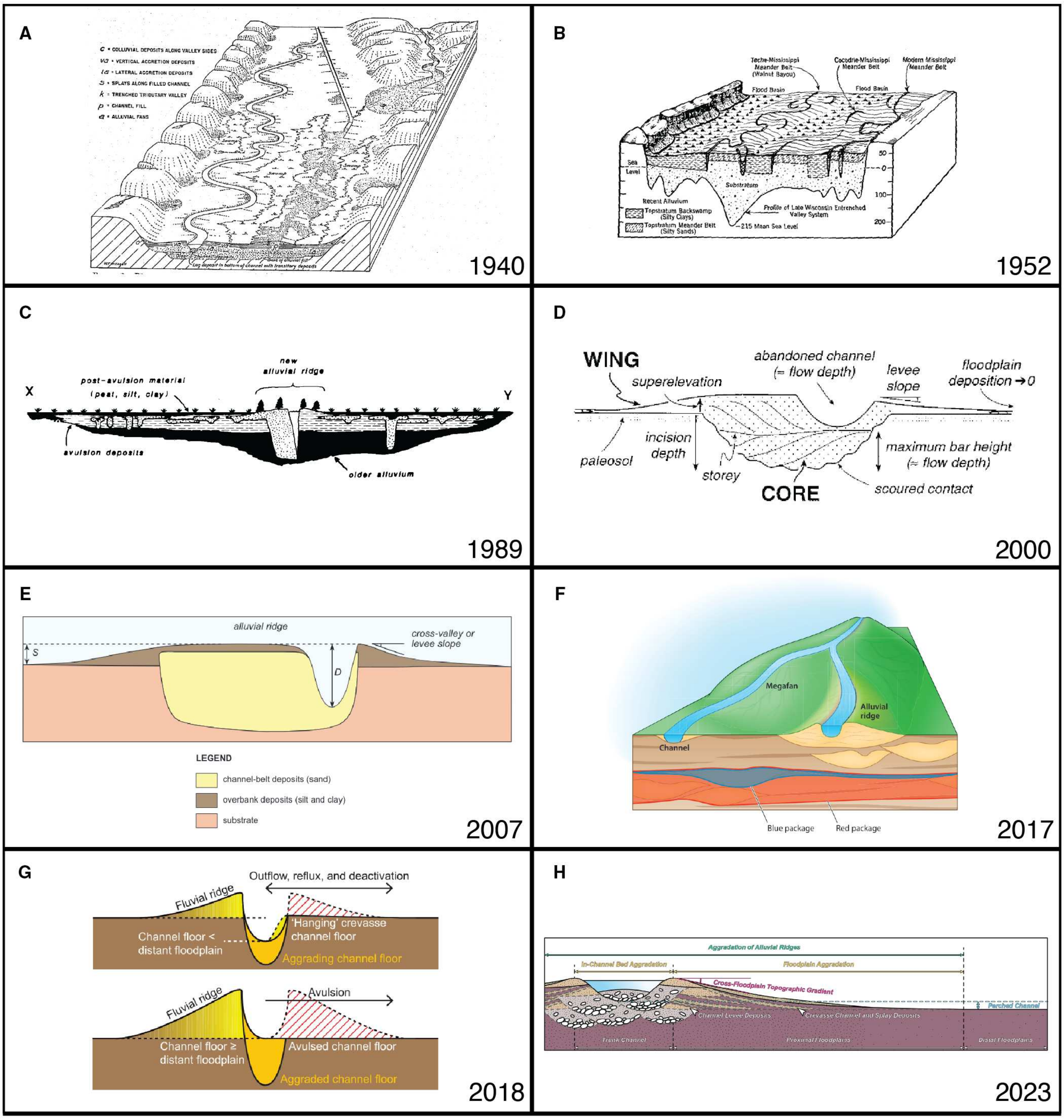

Fig. 1. Selected conceptual diagrams illustrating the evolution of scientific understanding of alluvial ridge morphology and formation. The panels show a progression from early recognition of ridges as large-scale landforms built by channel migration and levee-building (A, B), to process-based cross-sections that quantify the geometry driving avulsion (C, D, E, F), and finally to modern views emphasising their internal complexity and dynamic evolution through processes like crevasse splay aggradation (G, H). Schematics from: (A) Happ *et al.* (1940), (B) Fisk (1952), (C) Smith *et al.* (1989), (D) Mohrig *et al.* (2000), (E) Gouw (2007), (F) Hajek & Straub (2017), (G) Van Toorenenburg *et al.* (2018) and (H) Lee & Gihm (2023).

specific field studies. The fundamental barrier was practical: systematically measuring these vast, often remote landforms was intractable before the advent of global satellite datasets, and even for more accessible ridges, measuring their topography under thick riparian vegetation was not feasible. We therefore have a poor understanding of how alluvial ridge morphology varies across depositional environments and what controls this diversity.

Restricted by sparse spatial data, early quantitative studies relied on heuristic models of ridge geometry. The most prevalent form is the exponential decay profile, derived from diffusion-based models of overbank sediment transport (James, 1985; Pizzuto, 1987). This model produces a simple concave flank and underpins early alluvial stratigraphy models (Bridge & Mackey, 1993; Mackey & Bridge, 1995; Howard, 1996; Törnqvist & Bridge, 2002). While originally describing deposit thickness, this functional form applies equally to surface topography, assuming negligible compaction—a necessary constraint for topographic analysis:

$$h(x) = h_0 e^{-\lambda x}$$

where $h(x)$ is the ridge height at a distance x from the crest, h_0 is the crest height, and λ is a decay constant. However, site-specific studies have consistently shown that this idealised concave model cannot capture the full spectrum of observed morphologies. Ridge flanks also exhibit quasi-linear (Cazanacli & Smith, 1998; Adams *et al.*, 2004; Aalto *et al.*, 2008; Barefoot *et al.*, 2026), polynomial (Hassenruck-Gudipati *et al.*, 2022), stretched-exponential (Day *et al.*, 2008; Swanson *et al.*, 2008) and distinctly convex 'shouldered' profiles (Cazanacli & Smith, 1998; Ferguson & Brierley, 1999; Aalto *et al.*, 2008; Pizzuto *et al.*, 2008). This geometric diversity occurs because flank shape is modulated by local mechanisms, including advective transport, bedload contributions and vegetation trapping (Adams *et al.*, 2004; Filgueira-Rivera *et al.*, 2007; Pizzuto *et al.*, 2008; Branß *et al.*, 2022). Consequently, we do not know the characteristic shapes of alluvial ridges on avulsing rivers. Establishing a geometric baseline for their morphology is a critical first step towards building more accurate models of overbank deposition and avulsion.

Establishing this baseline is now possible with the recent availability of a global, bare-earth digital elevation model (Hawker *et al.*, 2022) and space-borne lidar altimetry (Neuenschwander *et al.*, 2020). While this dataset cannot distinguish individual, event-scale levees from the broader, time-integrated ridge structures they compose, it effectively captures the composite near-channel topography that guides avulsions and their pathways (Gearon *et al.*, 2024). We therefore adopt an inclusive approach, referring to these discernible aggradational features collectively as 'alluvial ridges'. We use these data to provide a systematic characterisation of alluvial ridge morphology.

METHODS

Data acquisition and study site characterisation

The primary dataset consists of topographic transects from 14 globally distributed river systems from Gearon & Edmonds (2025). We restrict the analysis to these systems for a critical reason: the measured topography reflects pre-avulsion conditions because these rivers experienced avulsion activity (in the satellite era 1984 CE to the present) after DEM acquisition (2011 to 2014) (Fig. 2). The 14 systems span three geomorphic settings—fans ($n = 3$), alluvial plains ($n = 8$) and deltas ($n = 3$)—and collectively contain 37 documented avulsion sites. The depositional setting (Fan, Alluvial Plain and Delta) for each river comes from Gearon & Edmonds (2025). These settings represent distinct stratigraphic and boundary conditions, ranging from the rift-margin deltas of the Linthipe River (Lyons *et al.*, 2011) and paleo-channel rich Río Ele floodplain (Vélez*et al.*, 2019) to the La Niña-controlled crevasse splays of the Río Cauca (Enciso *et al.*, 2016; Morón *et al.*, 2017) and the coarse fluvial fans of Musa River floodplain (Löffler, 1977). Table S1 lists exact SWORD reach identifiers and bounding coordinates for each analysed segment.

For these 14 systems, we extracted river-perpendicular elevation profiles from the 30 m resolution Forest and Buildings removed Copernicus DEM (FABDEM v1.2; Hawker *et al.*, 2022). We located these profiles using river centrelines and nodes spaced approximately 200 m apart in the SWOT River Database (SWORD v16; Altenau *et al.*, 2021). Following Gearon & Edmonds (2025), we extended profiles laterally up to 200 times the local channel width, capping the extension at 50 times for channels wider than 250 m, and sampled them at 30 m resolution. We defined reaches as sections between major tributaries, distributaries or non-avulsion-related morphological changes. If a reach contained multi-thread planforms or localised bifurcations, we selected the highest-order SWORD reach as the dominant hydraulic thread

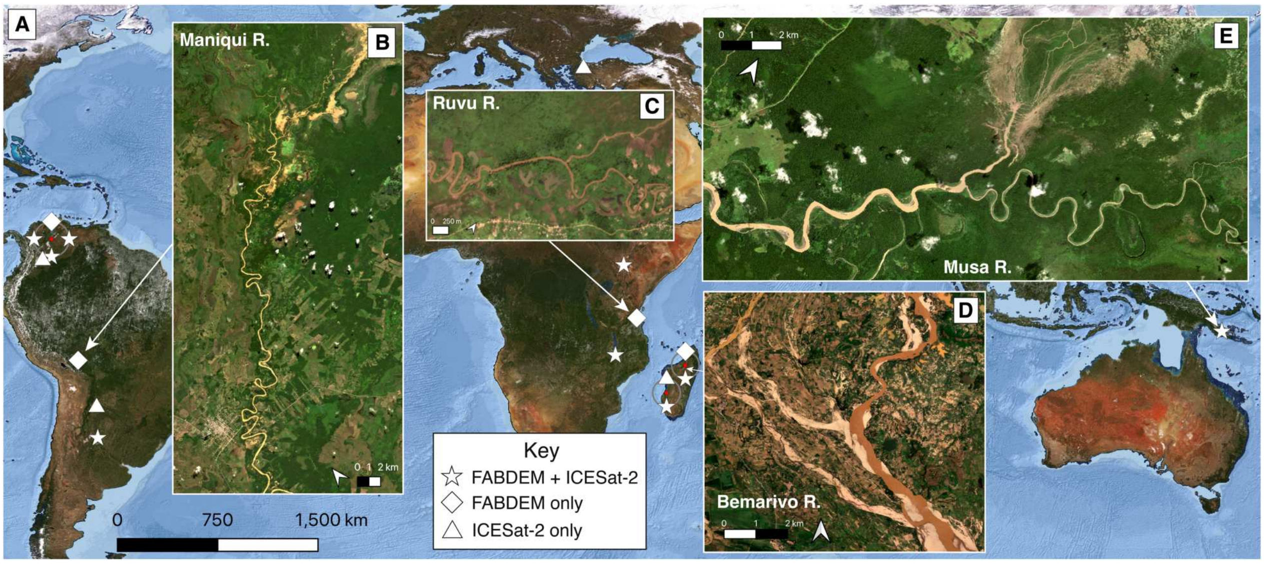

Fig. 2. Global distribution of the 14 avulsing river systems analysed in this study with DEM sampling. (A) Locations of the study sites are marked with white stars. (B–E) Satellite images showing four representative examples of recent avulsive events: (B) partial avulsion on the Maníqui River, Bolivia (2014); (C) partial annexational avulsion on the Ruvu River, Tanzania (2017); (D) full avulsion on the Bemarivo River, Madagascar (2018), and (E) a progradational crevasse splay on the Musa River, Papua New Guinea (2021). Basemap and all inset imagery are from Planet Labs PBC.

because it carries most of the discharge. We note that β and γ estimates carry greater uncertainty at these bifurcated sites because the channel depth and slope are more ambiguous.

Quantifying hydraulic geometry

The hydraulic parameters of the main channel used in this study consisted of slope, width and discharge. We obtained downstream water surface slope of the main channel (S_M) and water surface elevation from SWOT RiverSP Collection D for each SWORD-defined reach and node. We used reach-level SWOT-derived S_M where it: (1) passed the quality filter and (2) agreed within a factor of three with the FABDEM-derived slope and the prior SWORD estimate. Where both criteria were met, we replaced the DEM-derived prior slopes used in Gearon & Edmonds (2025) with direct SWOT observations; where either criterion failed, we retained the DEM-derived prior slope. We then removed remaining outliers exceeding three scaled median absolute deviations in log space across all reaches. Finally, we interpolated the cleaned reach-scale slopes to node spacing using a natural cubic spline in $\log_{10}(S_M)$ as a function of distance from outlet (Fig. S1).

Main channel width (W_M) was taken from the SWORD v16 prior, a Landsat-derived width at approximately mean-annual-discharge conditions from the Global River Widths from Landsat database (GRWL; Allen & Pavelsky, 2018, Altenau *et al.*, 2021).

We obtained the maximum long-term average monthly natural discharge of the main channel (Q_M) from the RiverATLAS dataset (Lehner & Grill, 2013; Linke *et al.*, 2019), which reports the flow of the highest month within an average year (1971 to 2000). Because this monthly value underestimates bankfull discharge, we applied the bias correction of Gearon *et al.* (2024): a power-law fit between RiverATLAS monthly maxima and 198 collocated field bankfull measurements (Trampush *et al.*, 2014). The corrected Q_M approximates channel-forming discharge; for application of the scaling relationships reported here, the appropriate input is an estimate of bankfull discharge. We then estimated bankfull channel depth (H_M) using the Boost-Assisted Stream Estimator for Depth (BASED), a gradient-boosted regression trained on 2562 global measurements of bankfull depth that takes the corrected Q_M, W_M and S_M as inputs (Gearon *et al.*, 2024; Gearon & Edmonds, 2025).

Quantifying alluvial ridge geometry

To extract alluvial ridge geometry from FABDEM elevation profiles, we defined two bounding features for each river cross-section: a ridge crest and a flood basin transition point (FTP) (Fig. 3). We identified the ridge crest as the local elevation maximum with positive topographic curvature, typically within 10 channel widths of the bank. We defined the FTP as the subsequent local slope break or lowest point before the next topographic high (Bridge & Leeder, 1979; Nanson & Croke, 1992). The profile between these two points constitutes a ridge 'flank'. We then applied three filtering criteria. Firstly, to minimise distortion, we excluded profiles oriented at low angles to sinuous channel belts. Second, in areas where the river impinged on one side of the valley, we analysed only one flank. Third, we omitted any cross-section with obvious topographic errors.

Using these bounding points, we calculated the primary geometric parameters for each flank. Notation and units for all morphometric and hydraulic variables used in the following analyses are summarised in the Appendix A. Alluvial ridge height (H_{AR}) is the vertical elevation difference between the crest and the FTP, and ridge half-width (W_{AR}) is the lateral distance between them. Together, these yield the characteristic ridge slope ($S_{AR} = H_{AR}/W_{AR}$). To contextualise these forms against the channel, we computed two dimensionless ratios: superelevation ($\beta = H_{AR}/H_M$) and gradient advantage ($\gamma = S_{AR}/S_M$). From these, we also calculated the avulsion potential ($\Lambda = \beta\gamma$). We then applied a two-tiered filtering strategy to the initial set of 9998 flanks. First, to enable geometric scaling analysis, we removed flanks with missing data ($n = 16$), insufficient lateral extent ($W_{AR} < 150$ m, approximately five DEM pixels, below which ridge slope is dominated by pixel-scale noise; $n = 1008$), non-physical values (e.g. $H_{AR} \leq 0$) or extreme dimensionless ratios (e.g. $\beta > 20$ and $\gamma > 1000, n = 13$, Fig. S2). Filtering reduced the initial 9998 flanks to 8970.

Because FABDEM is a machine learning product (Hawker *et al.*, 2022), we compared the ridge profiles to measurements from ICESat-2 in two ways. First, we provide a qualitative comparison. We compiled 16 high-resolution (~0.6 m point spacing) cross-sections from ICESat-2 ATL03 geolocated photon data (Figs 4 and 5). The associated ATL08 data product classifies these photons into ground and vegetation categories (Neuenschwander *et al.*, 2020), a workflow that accurately represents ground topography in forested terrain (Xing *et al.*, 2020; Gearon *et al.*, 2024). These cross-sections are river-perpendicular ground tracks from a variety of depositional environments (Table 1). Eleven examples come from rivers within the primary dataset, whereas five are from additional rivers selected for morphological variety. For 12 of the same rivers, we show the FABDEM-derived

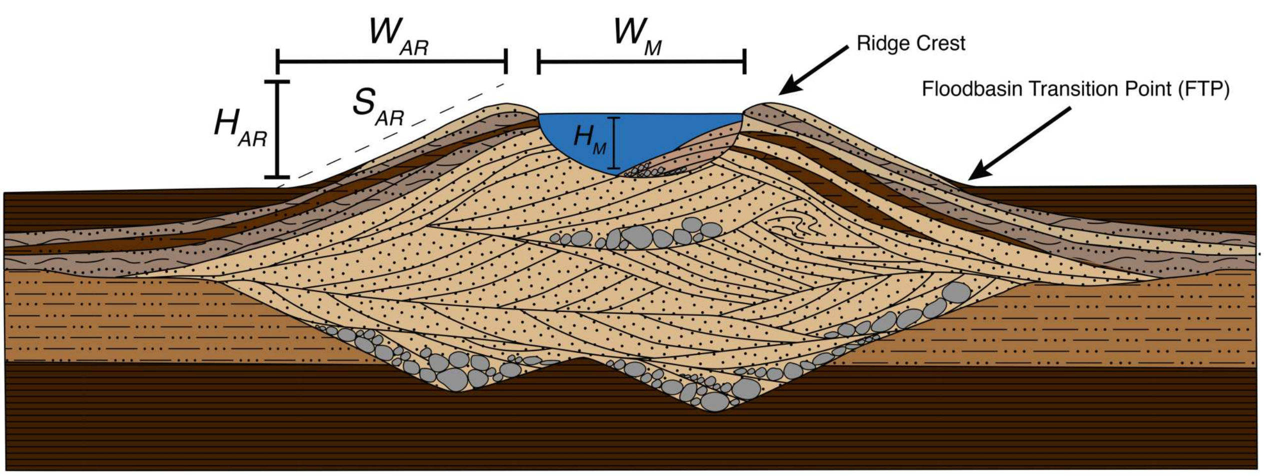

Fig. 3. Schematic cross-section of an alluvial ridge illustrating the morphometric parameters used in this study. Ridge height (H_{AR}) and half-width (W_{AR}) are measured from the crest to the flood basin transition point (FTP). Ridge slope (S_{AR}) is the ratio H_{AR}/W_{AR}. Channel depth (H_M), channel width (W_M), and channel slope (S_M) are reach-scale hydraulic properties. Superelevation $\beta = H_{AR}/H_M$, gradient advantage $\gamma = S_{AR}/S_M$, and avulsion potential $\Lambda = \beta\gamma$.

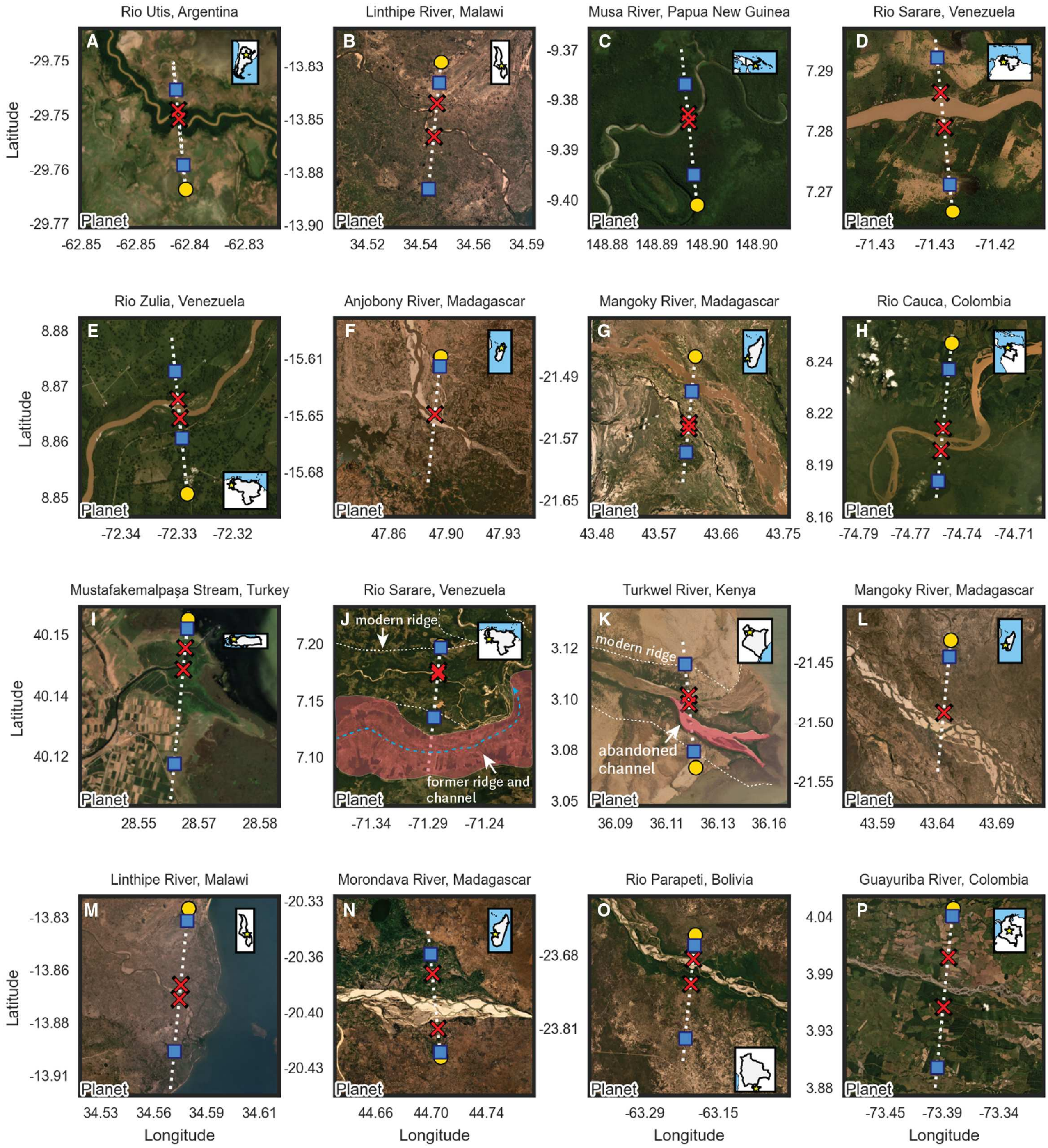

Fig. 4. Map views of the 16 ICESat-2 cross-sections shown in Fig. 5. Each panel (A–P) displays the ICESat-2 ground track as a white dashed line. The yellow dot marks the origin point ($x = 0$) of the corresponding profile in Fig. 5. Inset maps show the country of origin for each profile. All satellite imagery is from Planet Labs PBC, representing 3 m resolution monthly composites from the same month as the ICESat-2 data acquisition.

topography sampled along the same ICESat-2 track. Ridge crests and flood basin transition points are marked on each profile; cross-section coordinates are given in Table S3.

Second, we performed a quantitative comparison to estimate uncertainty in FABDEM ridge elevations. We sampled FABDEM along ICESat-2 ATL08 ground tracks across 14 rivers (~3.9

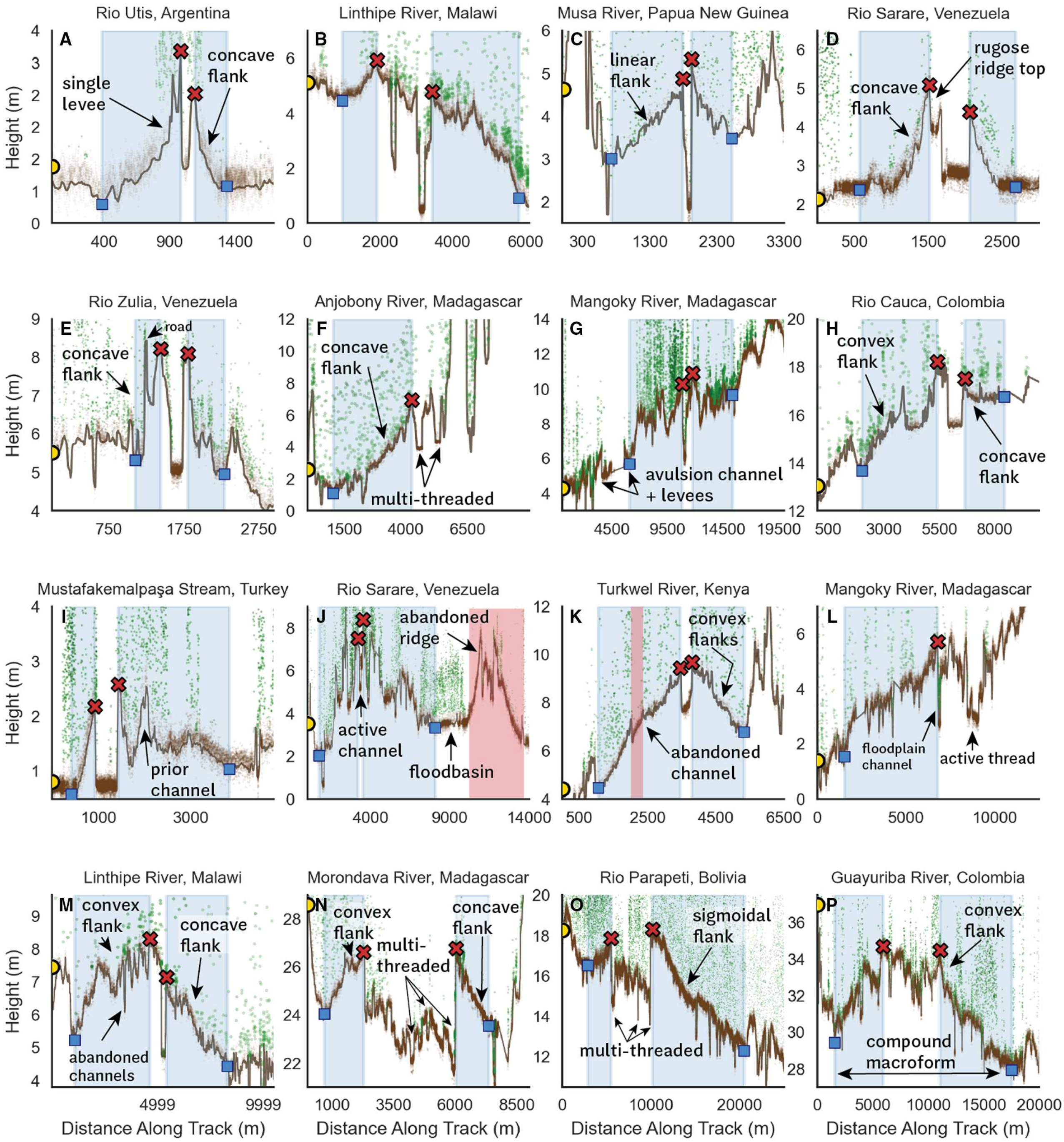

Fig. 5. Sixteen representative cross-sections derived from ICESat-2 ATL03 geolocated photon data, illustrating the diverse morphologies of alluvial ridges. Each profile (A–P) shows above-floodplain height versus along-track distance and is normalised to begin at the origin ($x = 0$, $y = 0$). The profiles are arranged by increasing lateral extent. The yellow dot at the origin of each cross-section is georeferenced to the corresponding satellite image in Fig. 4. Brown points indicate ground elevation photons, whereas green points represent canopy and vegetation returns as classified by the ATL08 algorithm (Neuenschwander *et al.*, 2020). Eleven of these profiles (A, B, C, D, E, F, G, H, K, L, M) are from rivers included in the primary analytical dataset (Fig. 2). Track orientations vary relative to the channel; along-track distance is used for visualisation.

Table 1. ICESat-2 illustrative profile locations.

Profile ID	River (country)	(Lat, Lon) WGS84	In DEM analysis?	Avulsion year	ICESat-2 acquisition date
A	Rio Utis (Argentina)	(−29.75, −62.84)	Yes	2017	2020-12-29
B	Linthipe River (Malawi)	(−13.86, 34.55)	Yes	2014	2019-06-09
C	Musa River (Papua New Guinea)	(−9.39, 148.89)	Yes	2021	2021-06-20
D	Rio Sarare (Venezuela)	(7.18, −71.28)	Yes	2022	2023-07-19
E	Rio Zulia (Venezuela)	(8.86, −72.33)	Yes	2022	2020-07-28
F	Anjobony River (Madagascar)	(−15.65, 47.89)	Yes	2018	2020-10-27
G	Mangoky River (Madagascar)	(−21.55, 43.61)	Yes	1978	2018-12-19
H	Rio Cauca (Colombia)	(8.20, −74.75)	Yes	2021	2020-06-04
I	Mustafakemalpaşa Stream (Turkey)	(40.14, 28.56)	No	2002	2020-08-05
J	Rio Sarare (Venezuela)	(7.29, −71.42)	No	2022	2019-01-18
K	Turkwel River (Kenya)	(3.09, 36.12)	Yes	2019	2022-09-14
L	Mangoky River (Madagascar)	(−21.51, 43.65)	Yes	2013	2024-09-07
M	Linthipe River (Malawi)	(−13.86, 34.57)	Yes	2014	2020-09-05
N	Morondava River (Madagascar)	(−20.37, 44.70)	No	2000	2024-08-09
O	Rio Parapeti (Bolivia)	(−23.75, −63.20)	No	1999	2022-09-14
P	Guayuriba River (Colombia)	(3.97, −73.39)	No	1987	2024-09-16

This table provides supplementary details for the 16 illustrative ICESat-2 topographic profiles shown qualitatively in Figs 4 and 5. Table entries correspond to panels A through P in the figures. We indicate whether the river shown in the profile is also one of the 14 systems from Gearon & Edmonds (2025) included in the main quantitative analysis, the approximate year of the most recent avulsion and the ICESat-2 acquisition date of the illustrative profile.

million points). Because the comparison is constrained to the satellite track geometry, it does not evaluate the specific ridge profiles analysed here; instead, it assesses the accuracy of FABDEM elevations at the reach scale. For each ridge flank, we masked in-channel points and removed anomalous returns where DEM-altimetry agreement exceeded $5 \times$ NMAD. NMAD is the normalised median absolute deviation (Höhle & Höhle, 2009) and is a robust measure of scatter that provides an outlier-resistant estimate of dispersion comparable to the standard deviation for Gaussian data.

The remaining ~3.7 million floodplain points yielded a median per-river NMAD of 0.64 m (Fig. 6A). Most observations exhibit low NMAD (<0.7 m) with moderate positive bias (~0.2 to 0.5 m), whereas the Fan setting shows substantially higher scatter (NMAD >1 m) and includes the largest outliers, indicating reduced precision relative to other settings (Fig. 6B). Because calculating H_{AR} requires subtracting the FTP elevation from the ridge crest elevation, measurement errors propagate into the difference. We independently derived H_{AR} values from FABDEM and ICESat-2 across 2296 crest–basin point pairs, which also yielded an empirical NMAD of 0.64 m (Fig. 6C and D). Because H_{AR} is the difference of two FABDEM elevations, uncorrelated pixel errors would propagate as $\sqrt{2} \cdot 0.64\ \text{m} = 0.91\ \text{m}$. The observed NMAD of 0.64 m is lower because spatially correlated DEM errors partially cancel in the crest-to-FTP difference. This spatial correlation means that ridge height measurements, which depend on elevation differences over short lateral distances, are more precise than per-pixel DEM accuracy would suggest.

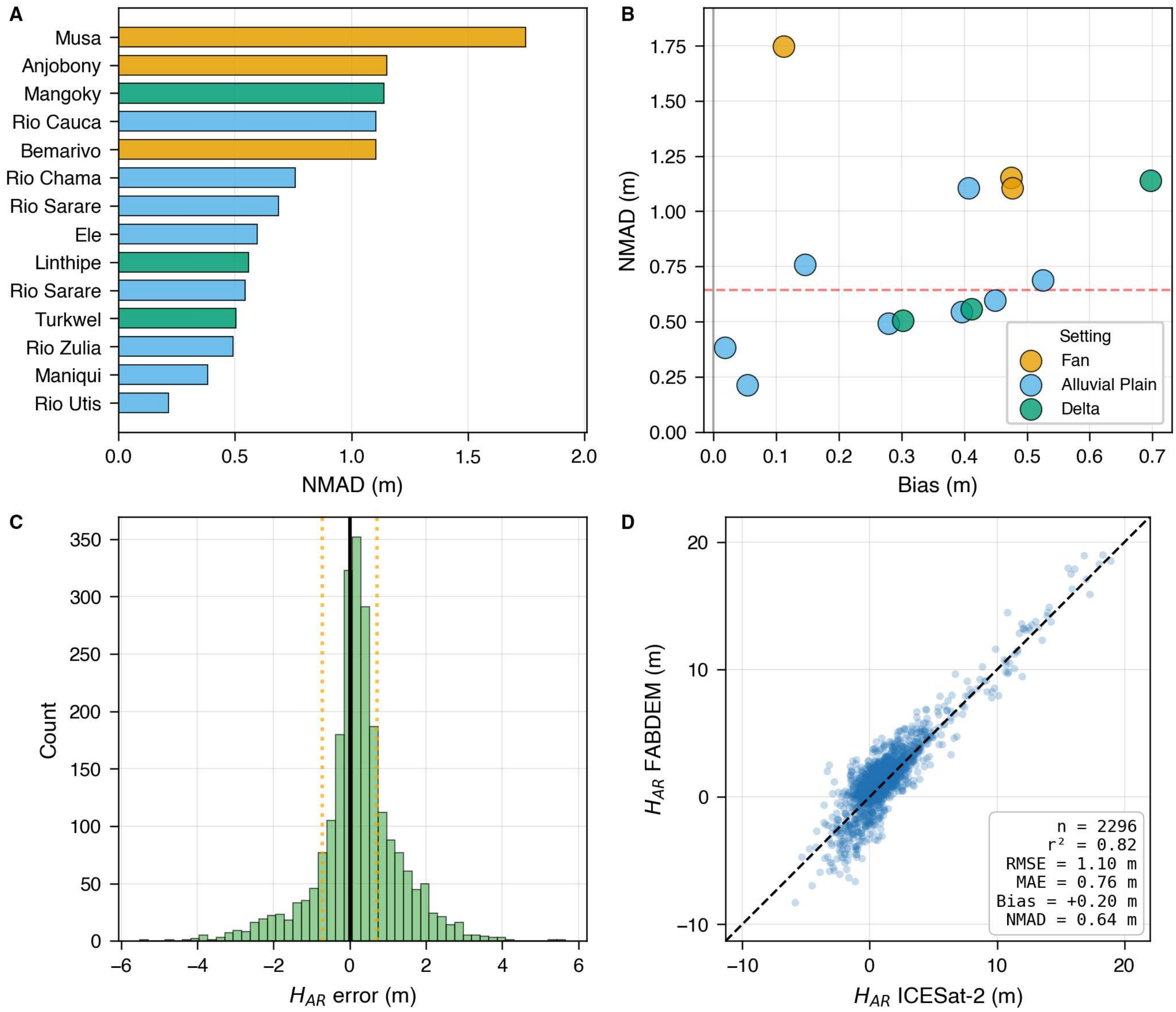

Fig. 6. Validation of flanks extracted from a bare-earth corrected global digital elevation model (FABDEM) floodplain elevations against ICESat-2 ATL08 altimetry across 14 study rivers (~3.7 million points after excluding channel zones and gross outliers). (A) Per-river normalised median absolute deviation (NMAD) of FABDEM–-ICESat-2 elevation differences; dashed red line marks the median across rivers (0.64 m). (B) Per-river bias vs. NMAD; FABDEM elevations are consistently higher than ICESat-2 (bias 0.01 to 0.73 m). (C) Histogram of ridge-height (H_{AR}) error from 2,296 crest–trough pairs; median = 0.20 m, NMAD = 0.64 m, below the theoretical independent-error bound of 0.91 m ($\sqrt{2} \cdot 0.64$ m) because spatially correlated FABDEM errors partially cancel across crest–trough pairs. (D) H_{AR} from FABDEM vs. ICESat-2 ($R^2 = 0.85$); dashed red line is 1:1. Eighty-three percent of flanks exceed the $1 \times$ NMAD detection floor.

To establish internal scaling, we regressed H_{AR} against W_{AR} across geomorphic settings (Alluvial Plain, Fan, Delta). To suppress DEM noise, we divided measurements into 15 equally populated quantile bins per environment, reducing the binned median standard error to 0.03 to 0.07 m. To identify external controls, we then related this ridge form to main channel width (W_M [m]), estimated bankfull depth (H_M [m]), water surface slope (S_M [−]), and bankfull specific discharge (Q_M/W_M [m²/s]). To make the $H_{AR} \propto W_{AR}^{\alpha}$ scaling non-dimensional for $\alpha \neq 1$, we normalised both variables by the gravitational flow-depth scale $\left(\frac{Q_M^2}{g}\right)^{\frac{1}{5}}$, the characteristic depth imposed by discharge Q_M under gravity g in wide open-channel flow (Parker *et al.*, 2007; Wilkerson & Parker, 2011).

$$H^{\star}_{AR} = \frac{H_{AR}}{\left(\frac{Q_M^2}{g}\right)^{\frac{1}{5}}} \text{ and } W^{\star}_{AR} = \frac{W_{AR}}{\left(\frac{Q_M^2}{g}\right)^{\frac{1}{5}}}.$$

We tracked the downstream evolution of avulsion potential (Λ) through its dimensional components (H_{AR}, S_{AR}, H_M, S_M) and dimensionless ratios (β, γ). We smoothed each profile with a Savitzky–Golay filter using a window of $\pm L_C$, the along-channel distance at which the autocorrelation of residual Λ falls to $1/e$ (Gearon & Edmonds, 2025). L_C is effectively the along channel length of a contiguous alluvial ridge. To verify that this choice does not bias avulsion-site identification, we repeated the Λ extraction across window half-widths ranging from 0.1 to 2.0 times L_C; median Λ near avulsion sites remains elevated above the river median for 9 of 14 rivers at all window sizes (Fig. S3). We characterised avulsion sites by averaging β and γ within a tighter window of $\pm 0.5 L_C$ around each documented avulsion.

To separate within-river from between-river structure in the β–γ state space, we computed per-river 1σ covariance ellipses and within-river OLS segments on log-transformed β and γ. We decomposed the between-river variation by regressing γ against S_M, β against H_{AR} and S_{AR} against S_M.

Curve fitting alluvial ridge flank morphology

Curve fitting the ridge profiles requires mostly artefact-free data. We isolated archetypal forms by applying a filter to remove any flank where large spikes elevated the maximum profile height more than 5% above the crest. This produced a subset of 6572 flanks for shape characterisation.

To quantify overall curvature, we standardised the 6572 archetypal flanks to a common reference frame (crest at the origin, FTP at zero elevation) and fit a second-order polynomial ($h(x) = a_{global}x^2 + Bx + C$) to each smoothed, normalised profile. We selected a quadratic model because it is the lowest-order polynomial capable of capturing continuous curvature. The leading coefficient (a_{global}) isolates the dominant curvature of the flank: its sign determines the direction of concavity, whereas its magnitude quantifies the intensity over the entire flank. Using a_{global}, we classified the flanks into three discrete forms: concave ($a_{global} > 0.1$), quasi-linear ($-0.1 \leq a_{global} \leq 0.1$) and convex ($a_{global} < -0.1$).

To test whether these geometries vary systematically by depositional setting, we computed a chi-squared test on the resulting contingency table (concave, quasi-linear, convex × fan, alluvial plain, delta), using Cramér's V to quantify the categorical effect size (Agresti, 2002; Table S4).

RESULTS

The varied forms of alluvial ridge topography

Alluvial ridges vary in form across all river planform types. The 16 ICESat-2 transects span seven single-thread (Fig. 4A, C, D, E, H, I and J) and nine multi-thread rivers (Fig. 4B, F, G, K, L, M, N, O and P), and their cross-sectional profiles trace a morphological continuum from concave, levee-like forms to kilometre-scale macroforms indistinguishable from the depositional systems they construct. Single-thread rivers produce the most levee-like profiles: sharp-crested, concave flanks that decay monotonically from the channel to the flood basin. This geometry matches the canonical natural levee described by Fisk (1944), Allen (1965), Ferguson & Brierley (1999), Adams *et al.* (2004), Branß *et al.* (2022) and others. The Río Utis in Argentina, part of the aggrading Chaco fan system (Iriondo, 1993; Lombardo, 2016), is the clearest example, with narrow, symmetric flanks on both sides of the channel (Figs 4A and 5A). Other single-thread systems share the concave decay but differ in symmetry and internal structure. The Río Sarare in the Venezuelan Llanos has sharp-crested, linear flanks that rise directly from an inundated flood basin (Nordin & Perez-Hernandez, 1989; Figs 4D and 5D). The Río Cauca, also a fan system, is subject to episodic La Niña flooding (Enciso *et al.*, 2016) and modified by dyke infrastructure (Bocanegra & Stamm, 2021), is wider, more asymmetric and more rugose than either the Utis or Sarare (Figs 4H and 5H).

Some ridges, on both single-thread and multi-thread rivers, develop convex shoulders near the channel and flanks that extend many channel-widths into the flood basin (Figs 4G, H, J, K, L, M, O, P and 5G, H, J, K, L, M, O, P). High sediment flux from the Owen Stanley Range builds the broad, low-relief linear forms of the Musa River (Fig. 5C, Löffler, 1977). The Río Zulia has a convex deposit adjacent to the active channel, with a local road forming a smaller left-bank peak (Fig. 5E). The Parapetí has high crest curvature that transitions into a sigmoidal decay (Fig. 5O).

In the dataset, braided rivers produce the broadest and most internally complex ridge forms. On the Morondava River in Madagascar, in-channel braid bars are flanked by ridges with contrasting morphologies: one concave, the other convex (Figs 4N and 5N). Similar compound ridges characterise the semi-arid Madagascan rivers in the dataset. Two Mangoky transects illustrate different expressions of this complexity: one crosses a channel abandoned before 1978, preserving the full paleo-channel form with steep inner banks and asymmetric flanks (Fig. 5G; Brooke *et al*., 2020), whereas another shows an active channel whose left convex flank hosts a secondary channel on its crest (Fig. 5L).

Where multiple generations of channelized flow have occupied the same corridor, modern ridges overprint older landforms to produce palimpsest topography. The Mustafakemalpasa Stream transect includes a former channel preserved as a raised triangular feature adjacent to the active ridge (Figs 4I and 5I). The wider Río Sarare transect (Figs 4J and 5J) crosses an active ridge studded with former channel courses, floodplain lakes, and paleo-channel fills as well as an abandoned ridge, which notably has very concave flanks in comparison to the active thread. They are separated by a flood basin. The Linthipe River profile records two scales of development: a larger, wider ridge with smaller, younger levees flanking the modern channel (Fig. 5B). Overbank topography in these systems is an amalgam of temporally distinct depositional events rather than the product of a single channel.

At the largest scale, alluvial ridges grade into the fans or deltas they construct. The Linthipe River in Malawi and the Guayuriba River in Colombia show multiple, superelevated, kilometre-scale convex macroforms (Figs 4M, P and 5M, P). These profiles define one end of the morphological continuum, where individual levee forms are no longer distinguishable from the composite depositional system.

FABDEM profiles sampled along these same ICESat-2 ground tracks reproduce the first-order ridge morphology on all 12 rivers (Fig. 7). Concave flanks appear on the Río Utis (Fig. 7A), broad convex shoulders on the Linthipe River (Fig. 7B,M), and compound multi-crested forms on the Mangoky River (Fig. 7G,L), all resolved at 30 m resolution. Where channels remained stable between DEM acquisition (2011 to 2014) and ICESat-2 overpass (2019 to 2024), the two datasets track within the 0.64-m NMAD established in Fig. 6 (e.g. Fig. 7A, E and F). Where profiles diverge, two categories of mismatch emerge. Some arise from DEM processing: FABDEM's hydroflattening algorithm introduces non-physical flat regions where it detects standing water (e.g. Fig. 7F and G), and localised elevation spikes from unremoved structures appear in individual transects (e.g. Fig. 7B, D, F and J). Others record real geomorphic change between acquisition epochs.

On the Turkwel River, an ICESat-2 transect from September 2022, 3 years after a December 2019 avulsion, captures the new channel already superelevating above its former course, while FABDEM preserves the pre-avulsion topography (Fig. 7K). On the Musa River, an avulsion between acquisition epochs placed the ICESat-2 transect across both the pre-avulsion channel and the new channel's incipient ridge (Figs 4C and 7C). The dense jungle environment of the Musa River and the observed aggradation around the abandoned course are consistent with a retrogradational avulsion where a downstream blockage causes an upstream-migrating dechannelisation wave that annexes and reroutes into a pre-existing channel (cf. Edmonds *et al*., 2022). On the Linthipe River, extreme upstream deforestation has accelerated sediment delivery to Lake Malawi over the last 40 years, and Landsat imagery records delta progradation that reshaped the floodplain between epochs (Fig. 7B and M; Ministry for Natural Resources, Energy and Mining, 2018). These temporal offsets are geomorphic signals, not DEM errors. This profile-to-profile variability is why we quantify ridge geometry statistically across thousands of flanks (Fig. 6) rather than rely only on individual transects.

Common morphologies of alluvial ridge flanks

The 6,572 FABDEM profiles exhibit a continuous spectrum of flank curvature ranging from strongly concave ($a_{global} > 0.1$) to quasi-linear ($-0.1 \leq a_{global} \leq 0.1$) to strongly convex ($a_{global} < -0.1$) (Fig. 8). The continuous distribution of these a_{global} values is unimodal and positively skewed (mean = 0.616) (Fig. 8A). Because positive coefficients denote concavity, this skew

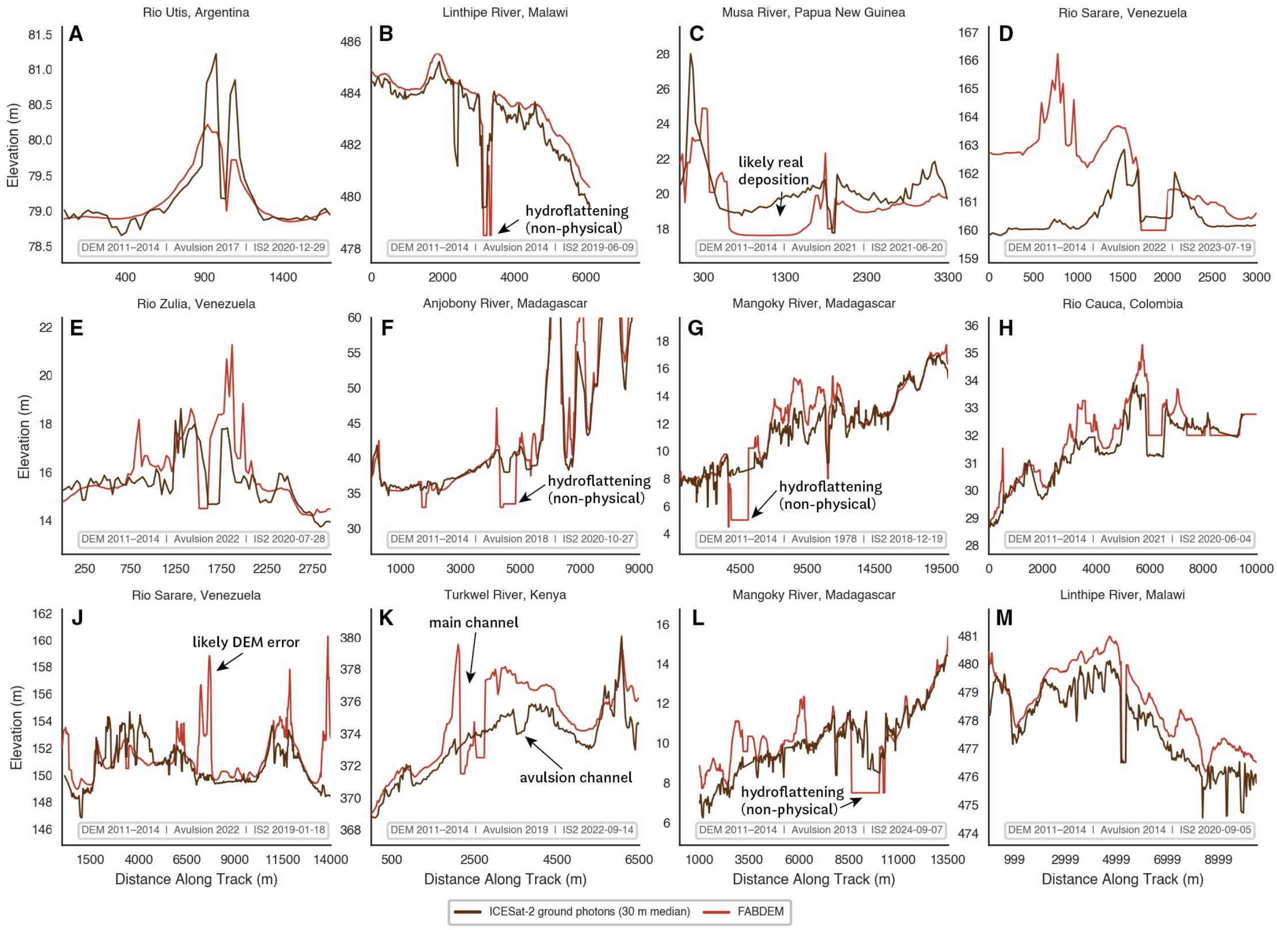

Fig. 7. Comparison of flanks extracted from a bare-earth corrected global digital elevation model (FABDEM) (red) and ICESat-2 ATL03 ground photon medians (black) across 12 study rivers. Each panel shows one river-perpendicular transect; panel letters correspond to those in Figs 4 and 5. Panels G and L show separate reaches of the Mangoky River; panels B and M show separate reaches of the Linthipe River. DEM acquisition dates (2011 to 2014), avulsion dates and ICESat-2 acquisition dates are annotated on each panel. The median per river normalised median absolute deviation between the two datasets is 0.64 m (Fig. 6). FABDEM artefacts include hydroflattening, where the algorithm flattens detected water surfaces into non-physical plateaus (e.g. F, G, L), and localised elevation spikes from unremoved structures (e.g. E, D, J, H). Other profiles show generally close agreement between the datasets (e.g. A, B). Panels where the profiles diverge more broadly (e.g. C, D, K, M) correspond to locations where channels migrated or avulsed between the DEM acquisition and the ICESat-2 overpass. Cross-section coordinates are provided in Table S3.

suggests the concave flank is the dominant morphological archetype.

High-resolution ICESat-2 altimetry independently validates this concave dominance (Fig. 8B). The validation dataset ($n = 28$) also yields a positive mean curvature ($a_{global} = 0.243$). While the FABDEM and ICESat-2 distributions are statistically distinct, the difference between their means produces a negligible effect size (Cohen's $d < 0.2$; Cohen, 1988). This minor effect size confirms that both topographical datasets capture the same underlying geometry.

Concave flanks are also the most common class in each setting individually: 56% on fans ($n = 1{,}003$), 64% on alluvial plains ($n = 4{,}629$), and 55% on deltas ($n = 940$). Within alluvial plains, the concave fraction ranges from 47% (Musa) to 78% (Río Utis), a wider spread than the 8-percentage-point difference between the three settings. A chi-squared test rejects independence between curvature class and geomorphic setting ($\chi^2 = 88.2$, $P < 10^{-3}$) but setting explains <1% of curvature variation (Cramér's V = 0.08; Table S4).

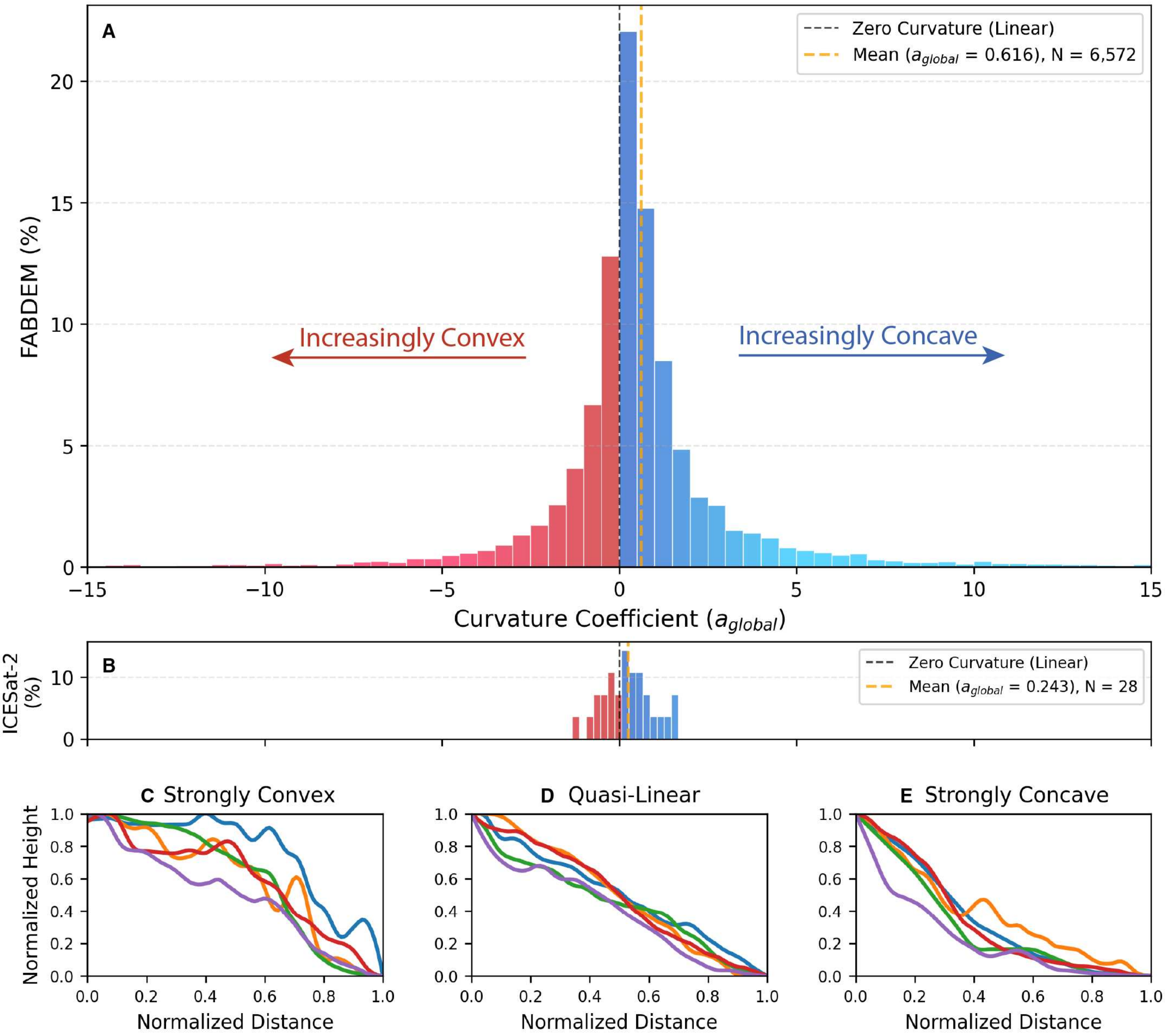

Fig. 8. Distribution and archetypes of alluvial ridge flank curvature. (A, B) Histograms of the global curvature coefficient (a_{global}) for the flanks extracted from a bare-earth corrected global digital elevation model ($n = 6{,}572$) and ICESat-2 ($N = 16$ cross-sections, $n = 28$ profiles) derived datasets, respectively. Positive values indicate concave-up curvature, whereas negative values indicate convex-up curvature. Red bars denote convex flanks, and blue bars denote concave flanks. The dashed black line indicates zero curvature (a linear flank), and the dashed orange line shows the mean of each distribution. (C–E) Each panel shows five examples of each class type, selected by quadratic fit and lightly smoothed for visualisation (Savitzky–Golay). Shape classification is based on the sign and magnitude of the quadratic coefficient (a) from a least squares fit to the smoothed flank. Both distance and height are normalised to [0, 1] for comparison.

Distributions and scaling relationships

The 8,970 DEM-sampled ridge flanks show broad statistical distributions in their geometric characteristics (Fig. 9). The median W_{AR} is 577 m (NMAD: 432 m), and median H_{AR} is 1.64 m (NMAD: 1.46 m). The derived dimensionless ratios also vary widely: median β is 0.24 (NMAD: 0.22), and median γ is 7.5 (NMAD: 7.1). Median Λ is 1.8 (NMAD: 2.0), just under the nominal avulsion threshold of 2 (Gearon *et al.*, 2024).

Despite this wide variance in absolute dimensions, alluvial ridges display a consistent internal geometry. Across all depositional environments, H_{AR} scales with W_{AR} as a power–law relationship $H_{AR} \propto W_{AR}^{0.75}$ (Fig. 10). This

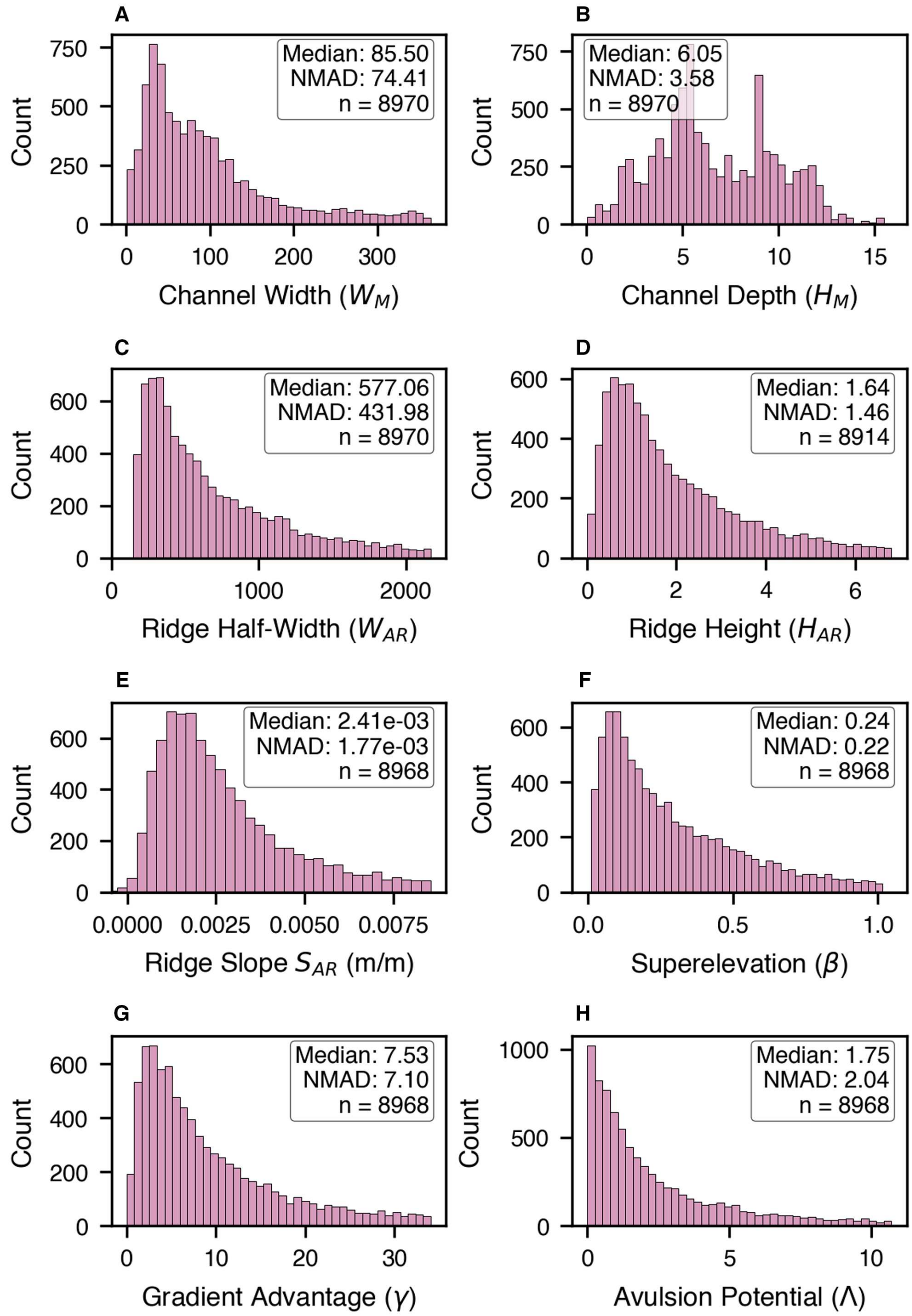

Fig. 9. Histograms showing the statistical distributions of key alluvial ridge and channel geometric parameters for the final dataset of 8,970 ridge flanks after removing outliers beyond 1.5 times the interquartile range for visualisation. Each panel reports the median, normalised median absolute deviation and the number of post-filtering data points (n). Parameters shown are (A) channel width (W_M), (B) estimated channel depth (H_M), (C) ridge half-width (W_{AR}), (D) ridge height (H_{AR}), (E) ridge slope (S_{AR}), (F) superelevation (β), (G) gradient advantage (γ) and (H) avulsion potential (Λ).

sub-linear scaling holds broadly, though the exponent varies by geomorphic setting: fan ($\alpha = 0.54$; $n = 1{,}401$), delta ($\alpha = 0.71$; $n = 1{,}222$) and alluvial plain ($\alpha = 0.84$; $n = 6{,}347$). In all three settings, scaling is sub-linear ($\alpha < 1.0$), but the exponent is lowest on fans and highest on alluvial plains. Because $\alpha < 1$, ridges grow wider faster than they grow taller. These results also hold at the within-river level as the same scaling shows up in a linear mixed effects (LME) model

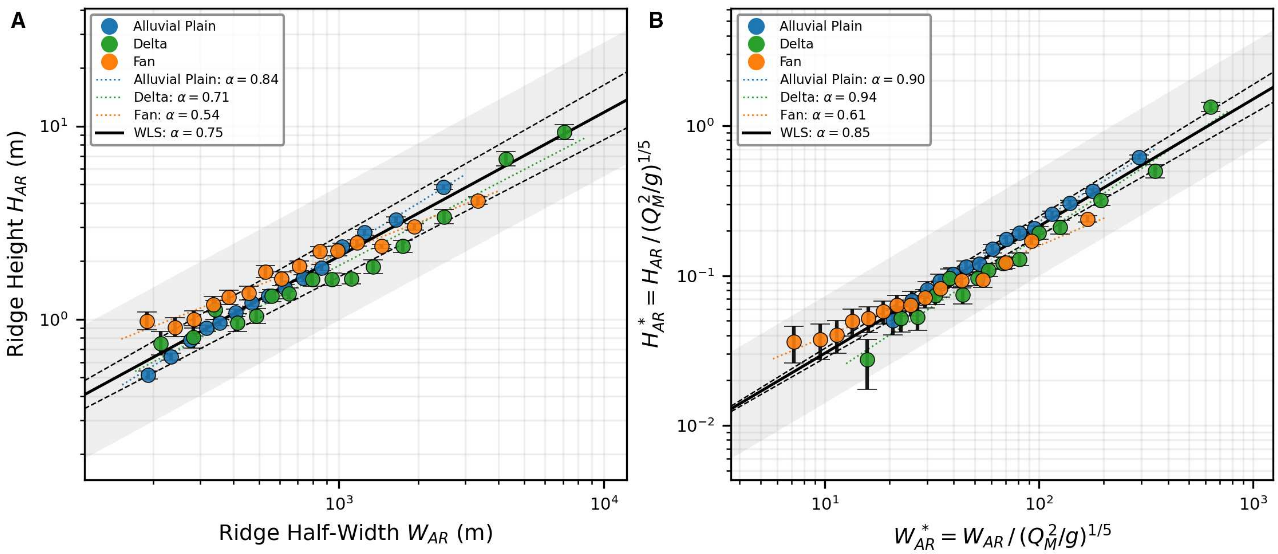

Fig. 10. Internal geometric scaling of alluvial ridges across geomorphic settings ($n = 8970$ flanks). Data are binned into 15 quantile (equal-count) bins of W_{AR} per setting. Coloured circles are bin medians with asymmetric SE_{median} error bars, estimated in log space and back-transformed. Dotted lines are WLS power-law fits to binned medians for each setting. The solid black line is an overall relation from inverse-variance weighting of the group slopes/intercepts; dashed lines show its slope confidence interval. A faint grey band indicates the 16% to 84% residual range about the overall line. Fit parameters appear in the legend.

with random intercepts (Table S2). The LME fixed effect slopes are shallower than the pooled estimates because the random intercepts absorb between-river variance, but six of seven relationships retain the same sign (Table S2). The exception is W_{AR} versus S_M, where between-river covariance between channel size and slope reverses the sign of the pooled trend: large, low-gradient rivers have wider ridges (positive pooled trend), yet within any single river, steeper reaches produce narrower flanks.

In dimensionless form, $H^{\star}_{AR} \propto W^{\star}_{AR}{}^{0.85}$ (Fig. 10B). The exponent steepens from 0.75 to 0.85 because Q_M covaries with W_{AR}; this covariance compresses the normalised horizontal axis. Per-setting dimensionless exponents are 0.61 (Fan), 0.90 (Alluvial Plain) and 0.94 (Delta); all three remain sub-linear ($\alpha^{\star} < 1$), though the Delta class approaches unity, indicating near-isometric scaling once the discharge effect is removed.

Ridge half-width scales with channel width but shows little sensitivity to hydraulic forcing. The strongest predictor of W_{AR} is channel width itself ($W_{AR} \propto W_M^{0.17}$, $R^2 = 0.46$, Fig. 11A), though the relationship varies by setting: alluvial-plain and deltaic rivers follow the global trend, whereas fan rivers show no width dependence. Channel slope explains less variance globally ($W_{AR} \propto S_M^{0.15}$, $R^2 = 0.13$ Fig. 11B), and the sign of the relationship reverses on deltas, where steeper channels correspond to narrower ridges. Specific discharge has no detectable global effect on ridge width ($W_{AR} \propto Q_M/W_M{}^{-0.05}$, $R^2 = 0.04$, Fig. 11C), although fan and deltaic rivers both exhibit negative scaling when fitted separately.

Ridge height responds to channel hydraulics more consistently than ridge width. Channel slope explains the most pooled variance of any ridge-height predictor ($H_{\text{AR}} \propto S_{\text{M}}{}^{0.39}$, $R^2 = 0.42$; Fig. 11E) and remains significant within individual rivers (LME slope 0.11, $P < 10^{-3}$; Table S2), with deltas exhibiting the steepest response. Specific discharge reinforces the slope signal: higher unit discharge corresponds to shorter ridges everywhere ($H_{\text{AR}} \propto (Q_{\text{M}}/W_{\text{M}})^{-0.19}$, $R^2 = 0.31$; Fig. 11F; LME slope -0.05, $P < 10^{-4}$). Deeper channels also build proportionally shorter ridges ($H_{\text{AR}} \propto H_{\text{M}}{}^{-0.25}$, $R^2 = 0.11$; Fig. 11D; LME slope -0.19, $p < 10^{-3}$), though the pooled signal is noisy because per-setting responses diverge: deltas show steep inverse scaling (-1.14), fans are intermediate (-0.42), and alluvial plains the shallowest (-0.30). These relationships collectively indicate that the largest alluvial ridges form alongside wide, shallow, steep channels with low specific discharge.

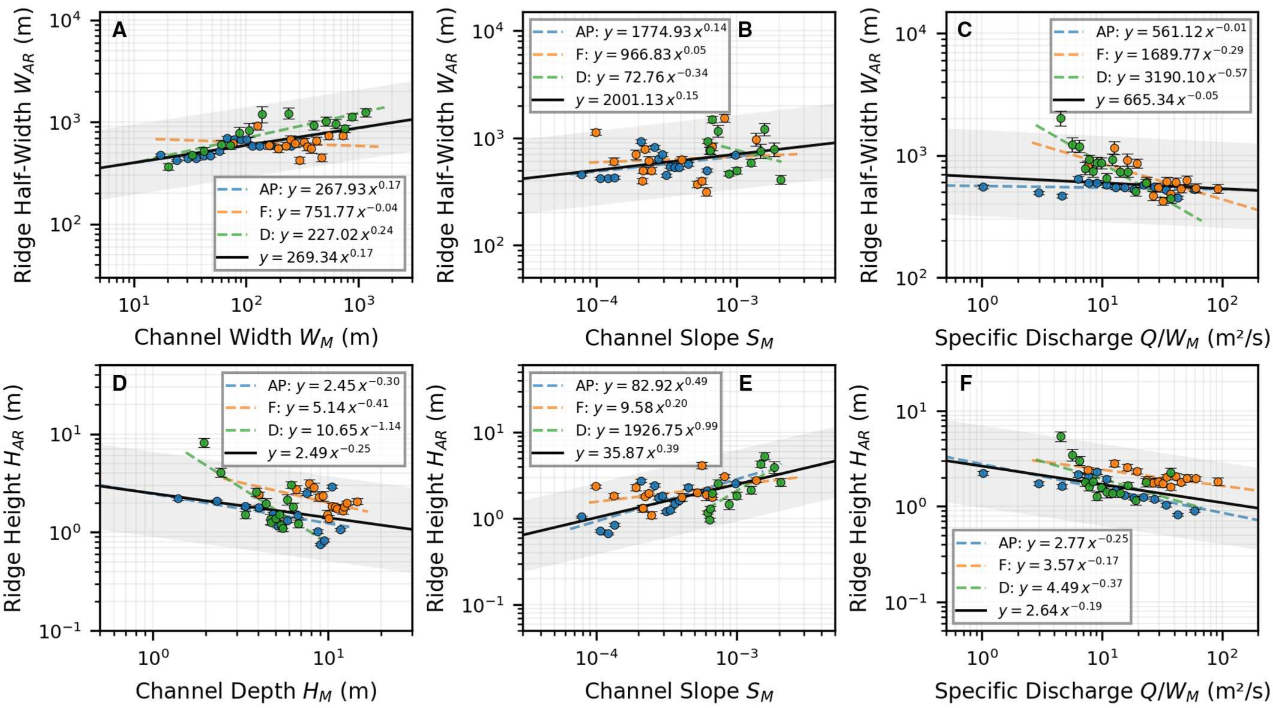

Fig. 11. Scaling between alluvial-ridge form and formative-channel properties across geomorphic settings ($n = 8{,}970$ flanks). Panels show: (A) ridge half-width $\mathrm{W_{AR}}$ vs channel width $\mathrm{W_M}$, (B) $\mathrm{W_{AR}}$ vs channel slope $\mathrm{S_M}$, (C) $\mathrm{W_{AR}}$ vs specific discharge $\mathrm{Q_M/W_M}$, (D) ridge height $\mathrm{H_{AR}}$ vs channel depth $\mathrm{H_M}$, (E) $\mathrm{H_{AR}}$ vs $\mathrm{S_M}$, (F) $\mathrm{H_{AR}}$ vs $\mathrm{Q_M/W_M}$. For each pair and setting, medians are plotted from 15 quantile (equal-count) bins of the independent variable with asymmetric $\mathrm{SE_{median}}$ error bars computed in log space and then back-transformed. Solid black lines are single WLS power-law fits to the aggregated binned medians weighted by bin counts ($\mathrm{n_{bins}}$); equations and R^2 are shown in each panel. Grey ribbons mark the 16% to 84% residual range around each overall fit.

βγ analysis results

Downstream evolution of relative geometry and avulsion potential

Across diverse depositional environments—including a fan (Bemarivo R.), a delta (Mangoky R.) and an alluvial plain (Río Zulia)—avulsion metrics exhibit consistent downstream spatial trends (Fig. 12). Main channel slope (S_M) strictly decreases and channel depth (H_M) increases downstream, whereas ridge height (H_{AR}) and flank slope (S_{AR}) vary only locally (Fig. 12A, D and G). Superelevation ($\beta = H_{AR}/H_M$) decreases downstream, whereas gradient advantage ($\gamma = S_{AR}/S_M$) increases (Fig. 12B, E and H).

The primary driver of avulsion potential ($\Lambda = \beta\gamma$) shifts along each river (Fig. 12C, F and I). Upstream reaches with high Λ are β-dominant, as on the Bemarivo fan. Downstream towards the delta front (e.g. Mangoky R.), decreasing β and increasing γ produce a transition to γ-dominance. On the Río Zulia alluvial plain, β and γ jointly peak, creating discrete high-Λ reaches (≈10) where superelevation and gradient advantage are simultaneously elevated.

βγ phase space relationships

The β–γ state space reveals that superelevation and gradient advantage covary positively within individual river cross-sections (Fig. 13A). Per-river covariance ellipses tilt towards the upper right for 13/14 rivers, indicating that flanks with anomalously high β also tend to have anomalously high γ on the same river. Avulsion sites, marked by ICESat-2-derived values, cluster around the $\Lambda \approx 2$ threshold, confirming that documented avulsions occur where both ratios are simultaneously elevated. The between-river decomposition isolates what drives each ratio. γ scales inversely with S_M ($r = -0.77$, $P = 0.001$; Fig. 13B), confirming that gradient advantage reflects downstream slope reduction rather than ridge steepening; ridge slope and channel slope are uncorrelated ($r = +0.14$, $P = 0.63$; Fig. 13D). β scales positively with ridge height ($r = +0.79$,

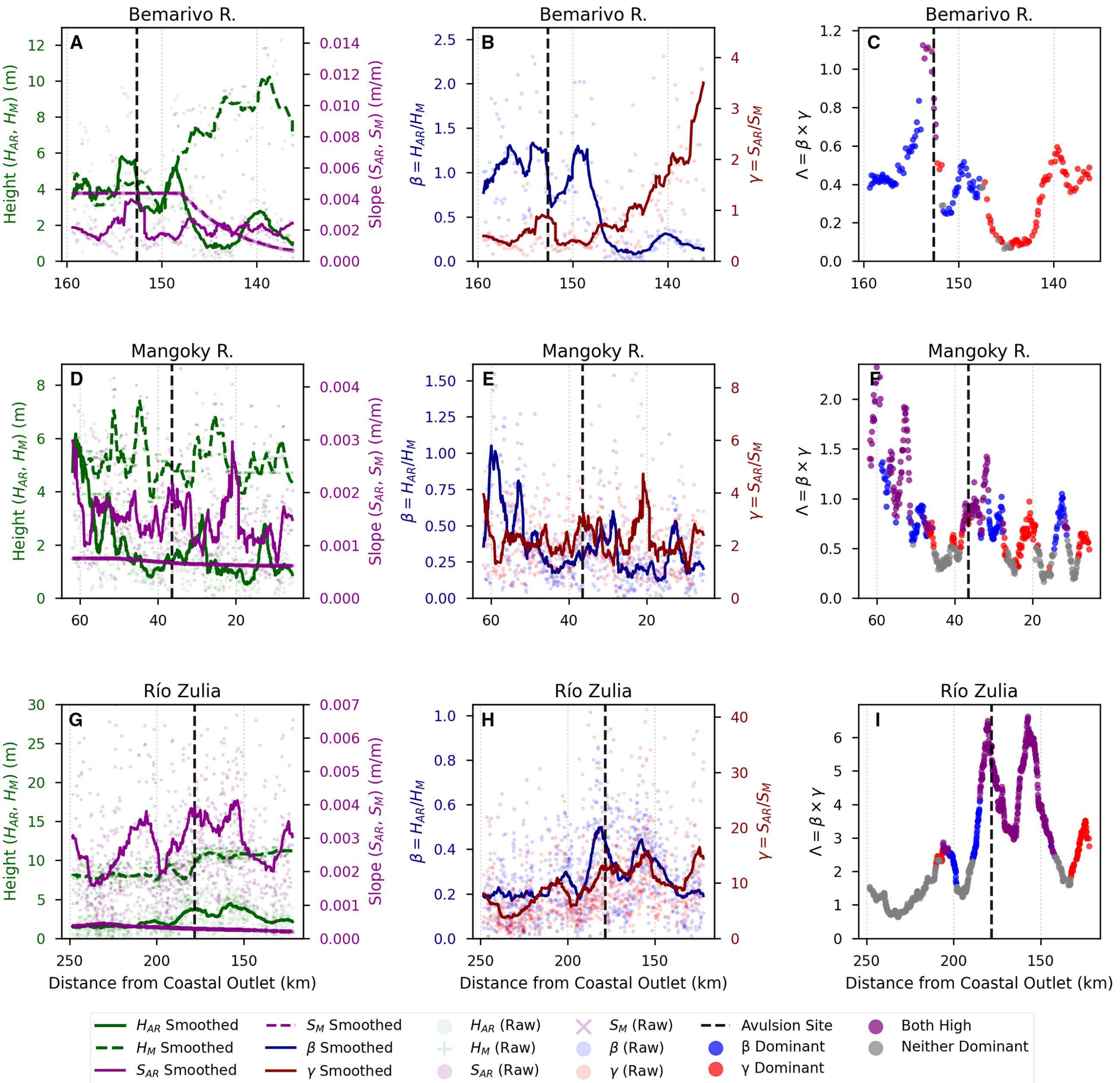

Fig. 12. Downstream evolution of dimensional and dimensionless geometric parameters for three representative rivers from different geomorphic settings: Bemarivo R., Madagascar (Fan); Mangoky R., Madagascar (Delta); and Río Zulia, Venezuela (Alluvial Plain). Each row represents one river and downstream is to the right. Left column (A, D, G): Raw measurements (faint points) and smoothed trends (solid/dashed lines) for dimensional variables: ridge height (H_{AR}), channel depth (H_M), ridge slope (S_{AR}) and channel slope (S_M). Vertical black dashed lines indicate the locations of recent avulsions. Centre column (B, E, H): Raw measurements and smoothed trends for the dimensionless ratios of superelevation (β) and gradient advantage (γ). Right column (C, F, I): Downstream profiles of avulsion potential (Λ), coloured by the dominant contributing factor relative to the reach-wide median values for β and γ. Blue indicates β-dominance, red indicates γ-dominance, purple indicates that both are high, and grey indicates neither is dominant. All smoothed series were filtered using a window size of $\pm L_C$, the characteristic correlation length-scale for each river's Λ series from Gearon & Edmonds (2025). The smoothing window ($\pm L_C$) controls the spatial resolution of the trend profiles; the tighter averaging window ($\pm 0.5\ L_C$) ensures all values used to characterise an avulsion site correlate strongly with that location ($r \geq 0.6$ at the window edge).

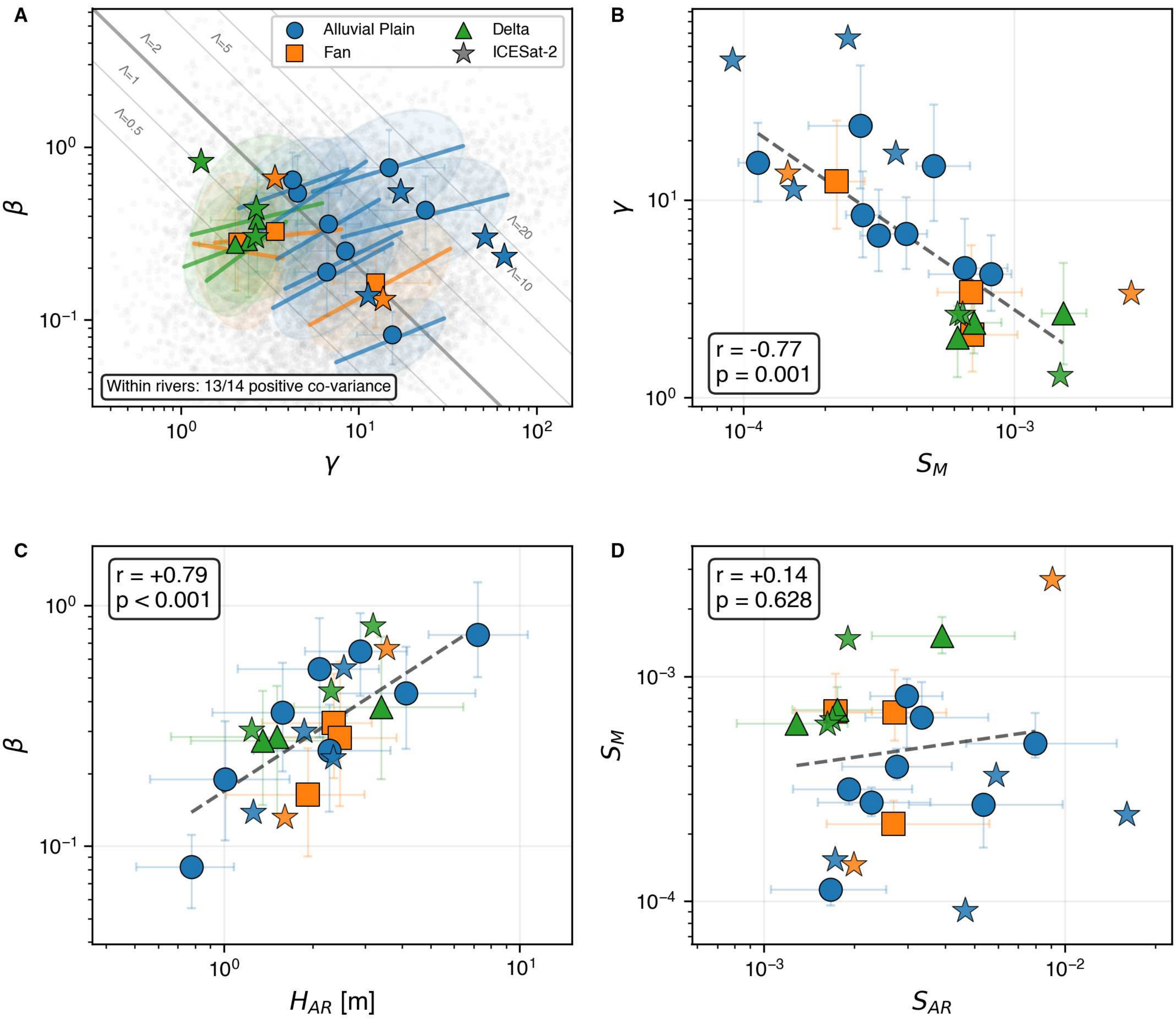

Fig. 13. Decomposition of the β–γ state space into dimensional components. (A) Per-river 1σ covariance ellipses and within-river OLS segments in β–γ space. Background contours mark constant Λ values; the $\Lambda = 2$ contour corresponds to the proposed avulsion threshold. Marker shape and colour encode geomorphic setting (circle/blue: alluvial plain; square/orange: fan; triangle/green: delta). Star markers show ICESat-2-derived values at documented avulsion sites. 13/14 rivers exhibit positive within-river β–γ covariance. (B) γ scales inversely with channel slope S_M ($r = -0.77$), indicating that between-river variation in gradient advantage reflects differences in channel gradient. (C) β scales positively with ridge height H_{AR} ($r = +0.79$), indicating that taller ridges drive higher superelevation. (D) Ridge slope S_{AR} and channel slope S_M are uncorrelated ($r = +0.14$, $P = 0.63$), confirming that γ variation arises from channel slope, not ridge steepness. IQR error bars shown in (B)–(D).

$P < 0.001$; Fig. 13C), confirming the direct link between superelevation and ridge aggradation.

DISCUSSION

Alluvial ridge growth modes

Alluvial ridge geometry integrates depositional events over geomorphic time (Fisk, 1944; Allen, 1965). Internal ridge scaling ($H_{AR} \propto W_{AR}^{0.75}$; Fig. 10) reveals the link between event-scale overbank flow and landform shape. This relationship holds globally: ridges grow wider faster than they grow taller. However, the scaling exponent α varies by setting, indicating distinct constructional modes. Because the sublinear scaling persists after controlling for discharge ($\alpha^{\star} = 0.85$), the pattern is intrinsic to the depositional process rather than an artefact of river size. Thus, α quantifies the efficiency of vertical aggradation relative to lateral spread.

These results appear paradoxical when viewed through the lens of fluvial mobility, the ratio of avulsion to lateral-migration time scales (Jerolmack & Mohrig, 2007). High mobility systems should rework sediment laterally to build wide, low-relief channel belts with a low α. Conversely, low-mobility systems, where vertical aggradation dominates, should produce tall, narrow ridges with high α. The data show the opposite: on fans built by channels that appear immobile in satellite images, the ridges are wide with the lowest α (Figs 4N, O, P and 5N, O, P).

The resolution lies not in the mobility of the channel itself, but in the scale of the landform being constructed. On alluvial plains, deposition concentrates within a distinct channel belt, often separated from the surrounding floodplain by low-lying interfluves (e.g. Figs 4J and 5J). The resulting alluvial ridge is a channel-scale feature whose geometry couples to belt-scale processes. Consistent with this coupling, ridge width correlates with channel width ($W_{AR} \propto W_M^{0.17}$) on alluvial plains. This focused deposition promotes vertical aggradation, producing high α values. These results suggest that the widening-dominant geometry reflects a universal property of overbank deposition: while discharge sets the hydraulic scale, lateral spread inherently outpaces vertical growth.

Conversely, immobile fan channels operate through frequent avulsion. In this nodally locked setting, distributive channel relocation builds width by 'tiling' successive channel belt deposits. Over geomorphic time, this process constructs a second-order composite fan macroform. Macroform geometry uncouples from the modern channel, as evidenced by the near-zero correlation between ridge width and channel width on fans ($W_{AR} \propto W_M^{-0.04}$). This construction prioritises lateral accretion over vertical aggradation at the landform scale, resulting in low α values. These low exponents reflect the emergent scaling of the compound landform rather than the properties of individual channel belts.

Hydraulic controls on alluvial ridge growth

Ridge height does not keep pace with channel depth. Across the dataset, H_{AR} scales inversely with H_M (Fig. 11D) and Q_M/W_M (Fig. 11F), while scaling positively with S_M (Fig. 11E). The largest channels—deep, low-gradient and carrying high discharge—build ridges that are small relative to their cross-sectional size. Ridge growth therefore depends not on total sediment load, which increases downstream, but on the efficiency with which sediment escapes the channel. Two mechanisms limit that escape in deep channels.

The first constraint is hydraulic. Downstream, H_M increases while S_M decreases, such that bed shear stress and shear velocity ($u_\star \propto \sqrt{H_M S_M}$) vary only weakly along the river profile (Leopold & Maddock, 1953; Singh *et al.*, 2003; Gleason & Smith, 2014). Consequently, the characteristic mixing timescale across the water column $H_M/u_\star$, increases as channels deepen. Classic suspension theory (Rouse, 1937) lacks this depth dependence because it expresses turbulent diffusivity as a function of relative rather than absolute height. Thus, if $u_\star$ and grain size remain constant, predicted bank-top sediment concentration is invariant with absolute depth.

Sand-laden rivers, however, develop density stratification that suppresses vertical turbulence and reduces mixing (Villaret & Trowbridge, 1991; Wright & Parker, 2004; Moodie *et al.*, 2022). Stratification breaks Rousean self-similarity, which steepens concentration profiles and reduces sediment load in the upper water column. This effect is strongest in deep, low-slope rivers that carry large suspended loads. As channels deepen, stratification reduces the suspended sediment concentration in surface waters available for overbank transport.

A parallel geometric constraint applies to bedload. In shallow channels, the saltation layer sits physically closer to the bank crest, allowing coarse grains to escape onto the floodplain during floods. In deep channels, the bedload transport zone becomes hydraulically isolated from the floodplain surface by the intervening water column. Bedload sediment has been documented as an important component of levee construction (e.g. James, 1985; Smith *et al.*, 1989; Cazanacli & Smith, 1998; Walling & He, 1998; Ferguson & Brierley, 1999; Filgueira-Rivera *et al.*, 2007; Han & Kim, 2022). Deep channels therefore lose bedload as a ridge-building mechanism.

We hypothesize that these constraints—reduced near-surface concentration from stratification (Villaret & Trowbridge, 1991) and bedload sequestration beneath deep water columns—limit the sediment mass available for overbank transport. This explains the inverse H_{AR}–H_M scaling and why deep channels build comparatively shorter ridges than shallow channels.

While local factors modulate overbank deposition, these relationships suggest that ridge dimensions are constrained by the physical difficulty of sediment export from deep, low-gradient channels.

Inverse H_{AR}–H_M scaling implies that deep channels produce proportionally shorter ridges relative to their lateral extent: a 'short and wide' architecture. The sub-linear exponent ($\alpha = 0.75$) is consistent with the temporal sequence of natural levee construction observed in the field. Maximum flood stage sets a physical ceiling on levee height, so crest-overtopping floods preferentially aggrade the proximal levee face early in ridge development (front-loading; Filgueira-Rivera *et al.*, 2007). Once that ceiling is reached, subsequent sub-bankfull floods aggrade the distal levee and extend width (back-loading), so that width accumulates long after height saturates (Shen *et al.*, 2015).

Fluvial sandbodies in the stratigraphic record also show sub-linear width–thickness scaling (Gibling, 2006), but preserved channel bodies and surface ridge relief are not equivalent measurements. The stratigraphic implication is therefore comparative rather than universal. Within a basin, ridges associated with deeper channels should preserve higher width-to-thickness ratios than ridges associated with shallower channels, all else equal. That pattern would indicate that modern ridge scaling survives burial into avulsion-generated channel-belt architecture.

Spectrum of alluvial ridge morphologies and their process signatures

Beyond geometric scaling, the cross-sectional shape of an alluvial ridge records something about the forces that shaped it, yet its form is highly variable, indicating differences in formative processes. This morphological diversity reflects underlying differences in channel planform, sediment supply and overbank flow physics. The sharp-crested, narrow ridges on the Río Utis, for example, likely result from a low-mobility channel that experiences regular floods with fine, cohesive sediment, generating a single, coherent levee set (Iriondo, 1993). In contrast, the semi-arid Madagascan rivers in the dataset experience highly variable discharge and are more mobile (Figs 4F, G, L, N and 5F, G, L, N). During extreme floods, these rivers mobilise significant suspended sediment that builds broad, advection-dominated forms (Aldegheri, 1972; Adams *et al.*, 2004; Pizzuto *et al.*, 2008). Other systems exhibit compound behaviours. The Sarare River appears to be both mobile in the migratory sense and vertically aggrading (Fig. 5J). Its profile reveals multiple, convex former river courses, as well as a paleo-ridge, suggesting a history where lateral migration and avulsive relocation have created a complex, multi-crested ridge and flood basin topography.

This morphological spectrum has direct implications for process-based models of ridge formation. Overbank depositional models based on diffusion or simple advection of suspended sediment predict concave, exponentially decaying profiles (James, 1985; Pizzuto, 1987). While concave flanks are the most common form in the dataset, they represent only around half of the observed morphologies. The significant number of quasi-linear and convex-up flanks demonstrates that this classic framework is incomplete.

Departures from this concave template likely record processes beyond simple diffusion (Adams *et al.*, 2004; Pizzuto *et al.*, 2008). Convex or quasi-linear flanks may arise where lateral channel migration or bank slumping erodes the proximal levee crest, where infrequent large floods transport coarser grains further onto the flank than typical overbank events, or where successive point-bar deposits stack on migrating bends. These mechanisms are not mutually exclusive; the continuous curvature spectrum suggests that most ridges reflect a superposition of diffusive settling and one or more of these modifying processes.

This analysis unifies these disparate observations. We show that avulsing rivers, with their high sediment loads, consistently host this entire morphological spectrum (Fig. 8). Morphological diversity is not an artefact of pooling across settings (Table S4); no single idealised profile is sufficient to capture these critical landforms.

Downstream evolution and avulsion dynamics

The new scaling relationships provide a geometric explanation for the recently identified source-to-sink changes in avulsion drivers (Gearon *et al.*, 2024). That work demonstrated a trade-off along depositional profiles: near mountain fronts, avulsions are driven by high β, whereas near coastlines, they are driven by a high γ. These findings reveal the underlying hydraulic and geometric controls driving this pattern. Standard hydraulic geometry predicts that channel depth increases and slope decreases downstream, which the scaling laws imply should suppress β and amplify γ. The three representative profiles in Fig. 12 illustrate this pattern, though individual rivers—which span only 30 to 50 km segments—deviate where local controls such as tributary junctions or avulsion nodes override the regional hydraulic gradient. The downstream decrease in superelevation ($\beta = H_{AR}/H_M$) is a direct consequence of the inverse scaling laws ($H_{AR} \propto Q/W_M{}^{-0.19}$ and $H_{AR} \propto H_M^{-0.25}$). As rivers move downstream, both specific discharge and channel depth typically increase. According to the scaling, both trends suppress alluvial ridge height (H_{AR}) and reduce β. Simultaneously, the downstream increase in the γ arises from the fundamentally different scales of the channel and its ridge. Channel slope (S_M) is a dynamic, regional property; it responds to basin-scale controls and varies by orders of magnitude from source to sink ($>10^{-2}$ to $<10^{-6}$). The alluvial ridge slope (S_{AR}), in contrast, belongs to a local, time-integrated landform. The data confirm that it is a more constrained property, with most values falling within a comparatively narrow range (Fig. 9E). A river's slope must decrease downstream, but the ridge slope, orthogonal to the river slope, is a more stable geometric property of the landscape. γ therefore systematically grows.

This trade-off establishes a physical hierarchy of controls on Λ, a concept with roots in historical discussions of avulsion controls (Slingerland & Smith, 1998; Mohrig *et al.*, 2000; Törnqvist & Bridge, 2002; Aslan *et al.*, 2005; Gouw, 2007). The basin-scale decline in channel slope (S_M) provides a first-order control, progressively increasing the gradient advantage (γ) downstream and pre-conditioning distal parts of a basin for avulsion. Against this backdrop, avulsions are triggered where local processes—such as channel choking, overbank sedimentation or obstructions—transiently elevate superelevation (β). This two-tiered control explains why avulsions are spatially localised. Avulsion sites consistently exhibit β and γ values that are anomalously high relative to their system's median trend, creating discrete, high-Λ 'hot spots' (Fig. 12) (see the more detailed exploration of avulsion hot spots in Gearon & Edmonds (2025)). The Río Zulia, where localised aggradation increases both β and γ over a characteristic length scale (Fig. 12H), illustrates this interplay.

The dimensional decomposition (Fig. 13B to D) explains why β and γ trend inversely along downstream profiles (Fig. 12) yet covary positively at individual cross-sections within a river. Channel slope accounts for most of the between-river variance in γ ($r = -0.77$; Fig. 13B): low-gradient rivers occupy high-γ space because their gentle S_M are easily exceeded by ridge flank slopes. Ridge height, meanwhile, accounts for most of the between-river variance in β ($r = +0.79$; Fig. 13C): rivers that build tall ridges have high superelevation. These two controls are linked through hydraulic geometry. Proximal rivers are steep and shallow with high sediment supply; they build tall ridges (high β) but have low γ because their steep channel slopes dominate the gradient ratio. Distal rivers are deep and gently sloped; their ridges are short relative to channel depth (low β), but γ is high because even modest ridge slopes exceed the vanishing channel gradient. The result is the inverse between-river β–γ correlation visible in Fig. 13A, where river medians track lines of roughly constant Λ.

Within a single river, the mechanism reverses. Local perturbations that elevate one ratio elevate the other: a reach where aggradation builds the ridge higher (raising β) is also a reach where the channel slope is locally reduced by backwater or obstruction (raising γ). 13/14 rivers in the dataset show this positive within-river covariance (Fig. 13A). The superposition of a negative between-river trend on positive within-river trends constitutes a Simpson's paradox in avulsion potential: pooling data across rivers without accounting for this structure would obscure the simultaneous elevation of β and γ that identifies avulsion-prone reaches.

Limitations and future directions

We acknowledge several limitations in this study. The reliance on manual identification of ridge features introduces operator subjectivity, though the ensemble-based approach mitigates random errors. The primary data limitations stem from the use of a global, static dataset. The 30 m resolution of FABDEM captures broader, time-averaged ridge forms rather than the fine-scale details of individual levees, and the static nature of the data provides only a single snapshot in time. Ridge heights (H_{AR}) reflect net topographic expression post depositional modification. Floodplains with highly compressible substrates lead to differential compaction beneath the heavier proximal ridge and the distal flood basin, which can reduce surface relief relative to the surrounding floodplain, so that measured H_{AR} underestimates the original depositional superelevation (cf. Törnqvist *et al.*, 2008; Nienhuis *et al.*, 2018). Where such effects are significant, the β values are conservative and the true depositional superelevation would be higher than reported here. The dataset does not include immobile deltaic channel systems (e.g. Rhine-Meuse, Po), where pinned distributaries may produce ridge geometries distinct from the mobile-to-avulsing systems studied here; characterising such systems represents an important extension for future work. More broadly, the requirement that avulsions postdate DEM acquisition (Gearon & Edmonds, 2025) restricts the delta class to small, relatively arid, fan-style systems ($n = 3$), which may not represent the hydraulic characteristics of larger, low-gradient deltas. Finally, while the analysis incorporates key hydraulic parameters, factors like sediment grain size, vegetation and subsurface geology could not be explicitly modelled and are only accounted for in aggregate. Despite these limitations, the consistency of the findings with sedimentological theory suggests the scaling relationships we identify hold across settings.

This work provides a direct path for future research. The increasing availability of high-resolution, time-series altimetry datasets will enable the direct observation of ridge growth over time. Such data will allow for rigorous testing of the scaling relationships identified here. Coupling these new observations with numerical simulations (e.g. Han & Kim, 2022; Han *et al.*, 2025) will provide an independent validation of the Λ threshold and a deeper understanding of the controls on its spatial and temporal variability.

CONCLUSIONS

This study provides a large-scale, quantitative characterisation of alluvial ridge morphology on 14 avulsing rivers. The sub-linear internal scaling and inverse ridge–channel relationships establish that ridge geometry is not independent of its formative channel: ridges on deep, low-gradient rivers are systematically thinner and wider. Together, these relationships explain the predictable downstream trade-off between superelevation-driven and gradient advantage-driven avulsion potential.

Ridge flank topography also reveals morphological diversity not captured by existing models. While concave flanks are the most common form, the prevalence of convex and quasi-linear shapes demonstrates that no single idealised profile can capture the near-channel topography that guides overbank flow. These morphologies, now systematically documented, challenge depositional models based on simple diffusion and point to a diversity of ridge-building mechanisms. This empirical baseline enables quantitative interpretation of fluvial landscapes and progress towards a physically grounded assessment of avulsion hazards in river systems worldwide.

ACKNOWLEDGEMENTS

Both authors were supported by the National Science Foundation (grant nos 2436929 and 2321056). The authors would like to thank Torbjörn Törnqvist, Youwei Wang and Gary Parker for their constructive review of the manuscript.

CONFLICT OF INTEREST

The authors declare no potential conflict of interests.

DATA AVAILABILITY STATEMENT

The data that support the findings of this study and the code used for analysis are available on Zenodo (10.5281/zenodo.19991228) and GitHub (github.com/jameshgrn/alluvial_ridge_morphology), respectively.

REFERENCES

Aalto, R., **Lauer, J.W.** and **Dietrich, W.E.** (2008) Spatial and temporal dynamics of sediment accumulation and exchange along Strickland River floodplains (Papua New Guinea) over decadal-to-centennial timescales. *J. Geophys. Res. Earth Surf.*, **113**, 1–4.

Adams, P.N., **Slingerland, R.L.** and **Smith, N.D.** (2004) Variations in natural levee morphology in anastomosed channel flood plain complexes. *Geomorphology*, **61**, 127–142.

Agresti, A. (2002) *Categorical Data Analysis*, 2nd edn. Wiley-Interscience, New York.

Aldegheri, M. (1972) Rivers and streams on Madagascar. In: *Biogeography and Ecology in Madagascar* (Eds Illies, J., Battistini, R. and Richard-Vindard, G.), Vol. **21**, pp. 261–310. Springer Netherlands, Dordrecht.

Allen, J.R.L. (1965) A review of the origin and characteristics of recent alluvial sediments. *Sedimentology*, **5**, 89–191.

Allen, J.R.L. (1978) Studies in fluviatile sedimentation: an exploratory quantitative model for the architecture of avulsion-controlled alluvial suites. *Sed. Geol.*, **21**, 129–147.

Allen, G.H. and **Pavelsky, T.M.** (2018) Global extent of rivers and streams. *Science*, **361**, 585–588.

Altenau, E.H., **Pavelsky, T.M.**, **Durand, M.T.**, **Yang, X.**, **Frasson, R.P.D.M.** and **Bendezu, L.** (2021) The Surface Water and Ocean Topography (SWOT) Mission River Database (SWORD): a global river network for satellite data products. *Water Resour. Res.*, **57**, e2021WR030054.

Aslan, A., **Autin, W.J.** and **Blum, M.D.** (2005) Causes of river avulsion: insights from the Late Holocene Avulsion History of the Mississippi River, U.S.A. *J. Sed. Res.*, **75**, 650–664.

Barefoot, E.A., **Gearon, J.H.** and **Edmonds, D.A.** (2026) O levee, where art thou? Measuring the abundance of natural river levees across the contiguous USA. *Case Rep. Med.*, **131**, e2025JF008642.

Blowe, D. (1820) A Geographical, Historical, Commercial, and Agricultural View of the United States of America: forming a Complete Emigrant's Directory Through Every Part of the Republic: particularising the States of Kentucky, Tennessee, Ohio, Indiana, Mississippi, Louisiana, and Illinois; and the Territories of Alabama and Missouri … East and West Florida, Michigan, and North-western … Likewise, an Account of the British Possessions in Upper and Lower Canada … *Edwards & Knibb*.

Bocanegra, R.A. and **Stamm, J.** (2021) Evaluation of alternatives to optimize the flood management in the department of Valle del Cauca. *J. Appl. Water Eng. Res.*, **9**, 1–19.

Branß, T., **Núñez-González, F.** and **Aberle, J.** (2022) Fluvial levees in compound channels: a review on formation processes and the impact of bedforms and vegetation. *Environ. Fluid Mech.*, **22**, 559–585.

Bridge, J.S. and **Leeder, M.R.** (1979) A simulation model of alluvial stratigraphy. *Sedimentology*, **26**, 617–644.

Bridge, J.S. and **Mackey, S.D.** (1993) A revised alluvial stratigraphy model. In: *Alluvial Sedimentation* (Eds Marzo, M. and Puigdefàbregas, C.), pp. 317–336. John Wiley & Sons, Ltd, Chichester, West Sussex, England UK.

Brooke, S.A.S., **Ganti, V.**, **Chadwick, A.J.** and **Lamb, M.P.** (2020) Flood variability determines the location of lobe-scale avulsions on deltas: Madagascar. *Geophys. Res. Lett.*, **47**, e2020GL088797.

Brown, S.R. (1817) The Western Gazetteer, or Emigrant's Directory, Containing a Geographical Description of the Western States and Territories … With an Appendix … By Samuel R. Brown. *H.C. Southwick*.

Cazanacli, D. and **Smith, N.D.** (1998) A study of morphology and texture of natural levees—cumberland marshes, saskatchewan, Canada. *Geomorphology*, **25**, 43–55.

Cohen, J. (1988) *Statistical Power Analysis for the Behavioral Sciences*, 2nd edn, p. 567. Lawrence Erlbaum Associates, Mahwah, NJ.

Court, U.S.S. (1893) Record, case no. 14,736.

Day, G., **Dietrich, W.E.**, **Rowland, J.C.** and **Marshall, A.** (2008) The depositional web on the floodplain of the Fly River, Papua New Guinea. *J. Geophys. Res. Earth Surf.*, **113**, 1–19. https://doi.org/10.1029/2006JF000622.

Edmonds, D.A., **Hajek, E.A.**, **Downton, N.** and **Bryk, A.B.** (2016) Avulsion flow-path selection on rivers in foreland basins. *Geology*, **44**, 695–698.

Edmonds, D.A., **Martin, H.K.**, **Valenza, J.M.**, **Henson, R.**, **Weissmann, G.S.**, **Miltenberger, K.**, **Mans, W.**, **Moore, J.R.**, **Slingerland, R.L.**, **Gibling, M.R.**, **Bryk, A.B.** and **Hajek, E.A.** (2022) Rivers in reverse: upstream-migrating dechannelization and flooding cause avulsions on fluvial fans. *Geology*, **50**, 37–41.

Enciso, A.M., **Carvajal-Escobar, Y.** and **Sandoval, M.C.** (2016) Análisis hidrológico de las crecientes históricas del río Cauca en su valle alto. *Ing. Compet.*, **18**, 47–58.

Ferguson, R.J. and **Brierley, G.J.** (1999) Levee morphology and sedimentology along the lower Tuross River, south-eastern Australia. *Sedimentology*, **46**, 627–648.

Filgueira-Rivera, M., **Smith, N.D.** and **Slingerland, R.L.** (2007) Controls on natural levée development in the Columbia River, British Columbia, Canada. *Sedimentology*, **54**, 905–919.

Fisk, H.N. (1944) *Geological investigation of the alluvial valley of the lower Mississippi River: U.S. Department of the Army, Mississippi River Commission*, p. 78. War Department, Corps of Engineers, Navy, Vicksburg, MS, USA.

Fisk, H.N. (1952) Mississippi river valley geology relation to river regime. *Trans. Am. Soc. Civ. Eng.*, **117**, 667–682.

Fisk, H.N., **United States, Mississippi River Commission** and **Waterways Experiment Station (U.S.)** (1947) *Fine-Grained Alluvial Deposits and their Effects on Mississippi River Activity*. Waterways Experiment Station, Vicksburg, Miss.

Frostick, L.E. and **Reid, I.** (1986) Evolution and sedimentary character of lake deltas fed by ephemeral rivers in the Turkana basin, northern Kenya. *Geol. Soc. London Spec. Publ.*, **25**, 113–125.

Gearon, J.H. and **Edmonds, D.A.** (2025) River avulsion precursors encoded in alluvial ridge geometry. *Geophys. Res. Lett.*, **52**, 1–9.

Gearon, J., **Martin, H.**, **DeLisle, C.**, **Barefoot, E.**, **Mohrig, D.**, **Paola, C.** and **Edmonds, D.** (2024) Rules of river avulsion change downstream. *Nature*, **634**, 91–95.

Gibling, M.R. (2006) Width and thickness of fluvial channel bodies and valley fills in the geological record: a literature compilation and classification. *J. Sed. Res.*, **76**, 731–770.

Gleason, C.J. and **Smith, L.C.** (2014) Toward global mapping of river discharge using satellite images and at-many-stations hydraulic geometry. *Proc. Natl. Acad. Sci. USA*, **111**, 4788–4791.

Gouw, M.J.P. (2007) Alluvial architecture of fluvio-deltaic successions: a review with special reference to Holocene settings. *Neth. J. Geosci.*, **86**, 129–146.

Hajek, E.A. and **Straub, K.M.** (2017) Autogenic sedimentation in clastic stratigraphy. *Annu. Rev. Earth Planet. Sci.*, **45**, 681–709.

Hajek, E.A. and **Wolinsky, M.A.** (2012) Simplified process modeling of river avulsion and alluvial architecture: connecting models and field data. *Sed. Geol.*, **257–260**, 1–30.

Han, J. and **Kim, W.** (2022) Linking levee-building processes with channel avulsion: geomorphic analysis for assessing avulsion frequency and channel reoccupation. *Earth Surf. Dyn.*, **10**, 743–759.

Han, J., **Kim, W.** and **Edmonds, D.A.** (2025) Assessing channel bank-height adjustments and flood frequency trends in a dynamic channel-levee evolution model. *Case Rep. Med.*, **130**, e2024JF008137.

Happ, S.C., **Rittenhouse, G.** and **Dobson, G.C.** (1940) *Some Principles of Accelerated Stream and Valley Sedimentation*. United States Department of Agriculture, Washington, DC.

Hassenruck-Gudipati, H.J., **Passalacqua, P.** and **Mohrig, D.** (2022) Natural levees increase in prevalence in the backwater zone: coastal Trinity River, Texas, USA. *Geology*, **50**, 1068–1072.

Hawker, L., **Uhe, P.**, **Paulo, L.**, **Sosa, J.**, **Savage, J.**, **Sampson, C.** and **Neal, J.** (2022) A 30 m global map of elevation with forests and buildings removed. *Environ. Res. Lett.*, **17**, 24016.

Heller, P.L. and **Paola, C.** (1996) Downstream changes in alluvial architecture; an exploration of controls on channel-stacking patterns. *J. Sed. Res.*, **66**, 297–306.

Höhle, J. and **Höhle, M.** (2009) Accuracy assessment of digital elevation models by means of robust statistical methods. *ISPRS J. Photogramm. Remote Sens.*, **64**, 398–406.

Hopkins, F.V. (1884) *Annual Report of the Secretary of war*. U.S. Government Printing Office, Washington, DC.

Howard, A. (1996) Modelling channel evolution and floodplain morphology. In: *Floodplain Processes* (Eds Anderson, M.G., Walling, D.E. and Bates, P.D.), pp. 15–62. John Wiley & Sons, Chichester.

Iriondo, M. (1993) Geomorphology and late Quaternary of the Chaco (South America). *Geomorphology*, **7**, 289–303.

James, C.S. (1985) Sediment transfer to overbank sections. *J. Hydraul. Res.*, **23**, 435–452.

Jerolmack, D.J. and **Mohrig, D.** (2007) Conditions for branching in depositional rivers. *Geology*, **35**, 463–466.

Karssenberg, D. and **Bridge, J.S.** (2008) A three-dimensional numerical model of sediment transport, erosion and deposition within a network of channel belts, floodplain and hill slope: extrinsic and intrinsic controls on floodplain dynamics and alluvial architecture. *Sedimentology*, **55**, 1717–1745.

Kidder, T.R. and **Liu, H.** (2017) Bridging theoretical gaps in geoarchaeology: archaeology, geoarchaeology, and history in the Yellow River valley, China. *Archaeol. Anthropol. Sci.*, **9**, 1585–1602.

Lee, K. and **Gihm, Y.S.** (2023) Overbank sedimentation and its influence on channel avulsion: examples of the Cretaceous Tando and Namyang basins in the mid-western part of the Korean Peninsula. *Geosci. J.*, **27**, 531–551.

Leeder, M.R. (1978) A quantitative stratigraphic model for alluvium, with special reference to channel deposit density and interconnectedness. In: *Fluvial Sedimentology* (Ed Miall, A.D.), *Canadian Society of Petroleum Geologists Memoir*, **5**, 587–596. Canadian Society of Petroleum Geologists (CSPG), Calgary, Alberta, Canada.

Lehner, B. and **Grill, G.** (2013) Global river hydrography and network routing: baseline data and new approaches to study the world's large river systems. *Hydrol. Process.*, **27**, 2171–2186.

Leopold, L.B. and **Maddock, T.** (1953) The hydraulic geometry of stream channels and some physiographic implications. *U.S. Geological Survey Professional Paper 252*, 57.

Linke, S., **Lehner, B.**, **Ouellet Dallaire, C.**, **Ariwi, J.**, **Grill, G.**, **Anand, M.**, **Beames, P.**, **Burchard-Levine, V.**, **Maxwell, S.**, **Moidu, H.**, **Tan, F.** and **Thieme, M.** (2019) Global hydro-environmental sub-basin and river reach characteristics at high spatial resolution. *Sci. Data*, **6**, 283.

Löffler, E. (1977) *Geomorphology of Papua New Guinea*, p. 195. CSIRO in Association with the Australian National University Press, Canberra.

Lombardo, U. (2016) Alluvial plain dynamics in the southern Amazonian foreland basin. *Earth Syst. Dynam.*, **7**, 453–467.

Lyons, R.P., **Scholz, C.A.**, **Buoniconti, M.R.** and **Martin, M.R.** (2011) Late quaternary stratigraphic analysis of the Lake Malawi Rift, East Africa: an integration of drill-core and seismic-reflection data. *Palaeogeogr. Palaeoclimatol. Palaeoecol.*, **303**, 20–37.

Mackey, S.D. and **Bridge, J.S.** (1995) Three-dimensional model of alluvial stratigraphy: theory and application. *J. Sed. Res.*, **65B**, 7–31.

Martin, H.K. and **Edmonds, D.A.** (2022) The push and pull of abandoned channels: how floodplain processes and healing affect avulsion dynamics and alluvial landscape evolution in foreland basins. *Earth Surf. Dyn.*, **10**, 555–579.

Ministry for Natural Resources, Energy and Mining (2018) *Republic of Malawi National Commitment to Achieve Land Degradation Neutrality*. Department of Forestry, Lilongwe, Malawi.

Mohrig, D., **Heller, P.L.**, **Paola, C.** and **Lyons, W.J.** (2000) Interpreting avulsion process from ancient alluvial sequences: Guadalope-Matarranya system (northern Spain) and Wasatch Formation (western Colorado). *GSA Bull.*, **112**, 1787–1803.

Moodie, A.J., **Nittrouer, J.A.**, **Ma, H.**, **Carlson, B.N.**, **Wang, Y.**, **Lamb, M.P.** and **Parker, G.** (2022) Suspended sediment-induced stratification inferred from concentration and velocity profile measurements in the Lower Yellow River, China. *Water Resour. Res.*, **58**, 1–24.

Morón, S., **Amos, K.J.**, **Edmonds, D.A.**, **Payenberg, T.H.D.**, **Sun, X.** and **Thyer, M.** (2017) Avulsion triggering by El Niño–Southern Oscillation and tectonic forcing: the case of the tropical Magdalena River, Colombia. *Geol. Soc. Am. Bull.*, **129**, 1–14.

Nanson, G.C. and **Croke, J.C.** (1992) A genetic classification of floodplains. *Geomorphology*, **4**, 459–486.

Neuenschwander, A., **Guenther, E.**, **White, J.C.**, **Duncanson, L.** and **Montesano, P.** (2020) Validation of ICESat-2 terrain and canopy heights in boreal forests. *Remote Sens. Environ.*, **251**, 112110.

Nicholas, A.P., **Aalto, R.E.**, **Sambrook Smith, G.H.** and **Schwendel, A.C.** (2018) Hydrodynamic controls on alluvial ridge construction and avulsion likelihood in meandering river floodplains. *Geology*, **46**, 639–642.

Nienhuis, J.H., **Törnqvist, T.E.** and **Esposito, C.R.** (2018) Crevasse splays versus avulsions: a recipe for land building with levee breaches. *Geophys. Res. Lett.*, **45**, 4058–4067.

Nordin, C. and **Perez-Hernandez, D.** (1989) *Sand Waves, Bars, and Wind-Blown Sands of the Rio Orinoco, Venezuela and Colombia*. U.S. Geological Survey, Reston, Virginia, USA.

Parker, G., **Wilcock, P.R.**, **Paola, C.**, **Dietrich, W.E.** and **Pitlick, J.** (2007) Physical basis for quasi-universal relations describing bankfull hydraulic geometry of single-thread gravel bed rivers. *Case Rep. Med.*, **112**, F4.

Piovan, S., **Mozzi, P.** and **Zecchin, M.** (2012) The interplay between adjacent Adige and Po alluvial systems and deltas in the late Holocene (Northern Italy). *Geomorphol. Relief Process. Environ.*, **2012**, 427–440.

Pizzuto, J.E. (1987) Sediment diffusion during overbank flows. *Sedimentology*, **34**, 301–317.
Pizzuto, J.E., **Moody, J.A.** and **Meade, R.H.** (2008) Anatomy and dynamics of a floodplain, Powder River, Montana, U.S.A. *J. Sed. Res.*, **78**, 16–28.
Rouse, H. (1937) Modern conceptions of the mechanics of fluid turbulence. *Trans. Am. Soc. Civ. Eng.*, **102**, 463–505.
Shen, Z., **Törnqvist, T.E.**, **Mauz, B.**, **Chamberlain, E.L.**, **Nijhuis, A.G.** and **Sandoval, L.** (2015) Episodic overbank deposition as a dominant mechanism of floodplain and delta-plain aggradation. *Geology*, **43**, 875–878.
Singh, V.P., **Yang, C.T.** and **Deng, Z.Q.** (2003) Downstream hydraulic geometry relations: 1. Theoretical development. *Water Resour. Res.*, **39**, 1337.
Slingerland, R. and **Smith, N.D.** (1998) Necessary conditions for a meandering-river avulsion. *Geology*, **26**, 435.
Slingerland, R. and **Smith, N.D.** (2004) River avulsions and their deposits. *Annu. Rev. Earth Planet. Sci.*, **32**, 257–285.
Smith, N.D., **Cross, T.A.**, **Dufficy, J.P.** and **Clough, S.R.** (1989) Anatomy of an avulsion. *Sedimentology*, **36**, 1–23.
Swanson, K.M., **Watson, E.**, **Aalto, R.**, **Lauer, J.W.**, **Bera, M.T.**, **Marshall, A.**, **Taylor, M.P.**, **Apte, S.C.** and **Dietrich, W.E.** (2008) Sediment load and floodplain deposition rates: comparison of the Fly and Strickland rivers, Papua New Guinea. *J. Geophys. Res. Earth Surf.*, **113**, 1–16. https://doi.org/10.1029/2006JF000623.
Törnqvist, T.E. and **Bridge, J.S.** (2002) Spatial variation of overbank aggradation rate and its influence on avulsion frequency. *Sedimentology*, **49**, 891–905.
Törnqvist, T.E., **Wallace, D.J.**, **Storms, J.E.A.**, **Wallinga, J.**, **van Dam, R.L.**, **Blaauw, M.**, **Derksen, M.S.**, **Klerks, C.J.W.**, **Meijneken, C.** and **Snijders, E.M.A.** (2008) Mississippi Delta subsidence primarily caused by compaction of Holocene strata. *Nat. Geosci.*, **1**, 173–176.
Trampush, S.M., **Huzurbazar, S.** and **McElroy, B.** (2014) Empirical assessment of theory for bankfull characteristics of alluvial channels. *Water Resour. Res.*, **50**, 9211–9220.
Vélez, A., **Jaramillo-J, A.**, and **Villamizar, V.A.** (2019) Geología del noreste del río Cravo Norte (margen izquierda), Colombia. In: *Colombia Diversidad Biótica XX* (Eds Rangel-Ch, J.O., Andrade, M.G., Jarro, C. and Santos, G.), p. 852. Universidad Nacional de Colombia, Bogotá.
Van Toorenenburg, K.A., **Donselaar, M.E.** and **Weltje, G.J.** (2018) The life cycle of crevasse splays as a key mechanism in the aggradation of alluvial ridges and river avulsion. *Earth Surf. Proc. Land.*, **43**, 2409–2420.
Villaret, C. and **Trowbridge, J.H.** (1991) Effects of stratification by suspended sediments on turbulent shear flows. *J. Geophys. Res. Oceans*, **96**, 10659–10680.
Walling, D.E. and **He, Q.** (1998) The spatial variability of overbank sedimentation on river floodplains. *Geomorphology*, **24**, 209–223.
Wilkerson, G.V. and **Parker, G.** (2011) Physical basis for quasi-universal relationships describing Bankfull hydraulic geometry of sand-bed rivers. *J. Hydraul. Eng.*, **137**, 739–753.
Wright, S. and **Parker, G.** (2004) Flow resistance and suspended load in sand-bed rivers: simplified stratification model. *J. Hydraul. Eng.*, **130**, 796–805.
Xing, Y., **Huang, J.**, **Gruen, A.** and **Qin, L.** (2020) Assessing the performance of ICESat-2/ATLAS multi-channel photon data for estimating ground topography in forested terrain. *Remote Sens.*, **12**, 2084.

APPENDIX A

Symbol	Description	Units
H_{AR}	Alluvial ridge height, measured from crest to flood basin transition point (FTP)	m
W_{AR}	Alluvial ridge half-width, measured from crest to flood basin transition point (FTP)	m
S_{AR}	Characteristic alluvial ridge slope, calculated as H_{AR}/W_{AR}	m/m
a_{global}	Global curvature coefficient from a quadratic fit to the ridge flank	m^{-1}
$h(x)$	Ridge height at a distance x from the crest in the exponential decay model	m
h_0	Ridge crest height in the exponential decay model	m
λ	Decay constant in the exponential decay model	m^{-1}
H_M	Mean depth of the main channel, estimated using the BASED model	m
W_M	Mean width of the main channel	m
S_M	Mean channel slope of the main channel along a reach	m/m
Q_M	Annual maximum natural discharge of the main channel (bias-corrected towards bankfull)	m^3/s
Λ	Avulsion potential, calculated as $\beta\gamma$	Dimensionless
β	Superelevation ratio, calculated as H_{AR}/H_M	Dimensionless
γ	Gradient advantage ratio, calculated as S_{AR}/S_M	Dimensionless
α	Scaling exponent in the power-law relationship $H_{AR} \propto W_{AR}{}^{\alpha}$	Dimensionless
L_C	Characteristic correlation length of the Λ series along a river	m

Manuscript received 29 November 2025; revision accepted 18 June 2026

Supporting Information

Additional information may be found in the online version of this article:

Figure S1. Assessment of Surface Water and Ocean Topography (SWOT)-derived slope and water surface elevation (WSE) quality and their effect on avulsion potential (Λ). (A–C) Channel slope versus distance from outlet for three example reaches—Rio Cauca (Fan), Río Ele (Alluvial Plain) and the Mangoky River (Delta)—showing raw SWOT reach-level slope observations (green diamonds) and cubic spline fits (blue lines) used to estimate local slope S_M. (D) SWOT slope versus flanks extracted from a bare-earth corrected global digital elevation model-derived slope for $n = 97$ reaches ($r = 0.62$); 93% of reaches agree within a factor of 3, with points colour-coded by geomorphic setting. (E) SWOT WSE versus ICESat-2 WSE for $n = 3222$ nodes ($r = 0.997$, $NMAD = 1.15$ m, $bias = -0.68$ m), showing near −1:1 agreement. (F) Λ computed with SWOT + ICESat-2 WSE versus Λ computed with ICESat-2-only WSE for $n = 4163$ flanks (median ratio = 1.000, r[log] = 0.984); Λ is invariant to WSE source.

Figure S2. Sensitivity of the $H_{AR} \sim W_{AR}$ scaling exponent to the superelevation (β) and gradient advantage (γ) filter thresholds. (A) Cumulative distribution of β across all flanks; the applied threshold $\beta_{max} = 20$ exceeds the observed range (maximum $\beta = 8.5$; 99th percentile = 2.3). (B) Cumulative distribution of γ; dashed red line marks $\gamma_{max} = 1000$ (maximum observed $\gamma = 981$). (C) Scaling exponent (blue circles, left axis) and percentage of flanks retained (orange squares, right axis) as β_{max} varies from 1 to 30; dashed red line at the applied threshold. The exponent shifts only when β_{max} falls below the 95th percentile. (D) Same as (C) for γ_{max} varying from 50 to 1500. In both cases, the applied thresholds exclude no more than 0.1% of flanks and leave the scaling exponent unchanged.

Figure S3. Sensitivity of avulsion-site Λ to the averaging window half-width. Each thin line shows the ratio of median Λ near a documented avulsion site to the river's background median, for one of 14 rivers, as the averaging window expands from ±0.1 to ±2.0 times the autocorrelation length scale (L_C). The blue envelope marks the interquartile range across all rivers; filled circles mark the cross-river median. The horizontal dotted line at 1.0 indicates no elevation above background. Avulsion-site Λ exceeds the river median for 9 of 14 rivers at every window size tested. Avulsion-site identification is therefore insensitive to the smoothing parameter. The dashed vertical line marks the default window (±0.5 L_C) used in this study.

Table S1. SWORD v16 reach identifiers, centroid coordinates, geomorphic setting and number of cross-sections for each study river. Reach IDs follow the SWORD v16 database (Altenau *et al.*, 2021). Settings are classified as Fan (F), Alluvial Plain (AP) or Delta (D).

Table S2. Linear mixed effects model results with random intercepts per river. Each row reports the fixed effect slope, standard error, 95% confidence interval and *P*-value for one scaling relationship ($n = 8970$ flanks across 14 rivers, except $H^*_{AR} \sim W^*_{AR}$ which uses $n = 8970$). Six of seven relationships retain the same sign as the pooled estimates. The exception is $W_{AR} \sim S_M$, where between-river covariance between channel size and slope reverses the sign of the pooled trend (see Discussion). W_{AR} scales positively with W_M and negatively with S_M; H_{AR} scales negatively with H_M and positively with S_M. The dimensionless relationship $H^*_{AR} \sim W^*_{AR}$ yields a within-river exponent of 0.62 (95% CI: 0.60 to 0.64).

Table S3. Coordinates and identifiers for the 12 flanks extracted from a bare-earth corrected global digital elevation model cross-sections shown in Fig. 7. Panel letters correspond to those in Fig. 5. Latitude and longitude are WGS 84 centroids of each transect. The cross_id is the internal pipeline identifier linking each profile to the elevation parquet files available at LINK.

Table S4. Per-setting and per-river curvature classification of flanks extracted from a bare-earth corrected global digital elevation model ridge flanks. Classification boundaries: concave ($a_{global} > 0.1$), quasi-linear ($-0.1 \le a_{global} \le 0.1$), convex ($a_{global} < -0.1$).